

ELEMENTARY LOOP STRUCTURES IN THE SOLAR CORONA ANALYZED FROM *TRACE* TRIPLE-FILTER IMAGES

MARKUS J. ASCHWANDEN AND RICHARD W. NIGHTINGALE

Lockheed Martin Advanced Technology Center, Solar and Astrophysics Laboratory, Department ADBS,
 Building 252, 3251 Hanover Street, Palo Alto, CA 94304; aschwanden@lmsal.com

Received 2005 June 6; accepted 2005 July 13

ABSTRACT

This study represents the first quantitative analysis of the multithread structure of coronal loops. We analyzed a set of 234 fine loop threads observed with *TRACE* triple-filter images at wavelengths of 171, 195, and 284 Å. The cross-sectional flux profiles are simultaneously forward fitted in all three filters with the superposition of a cospatial Gaussian and linear background functions. We fit a general multitemperature differential emission measure (DEM) distribution to each cross section, as well as the special case of a single-temperature or isothermal DEM. We perform these forward fits at $\approx 18,000$ loop positions and find that this geometric model could be fitted in ≈ 3500 cases (within a $\chi_{\text{red}} \leq 1.5$), while all other cases require more complex geometric models of the loop cross section, secondary loops, and background. The major result of this study is that the vast majority (84%) of the acceptable DEM fits are isothermal. Temperatures are measured over the whole sensitivity range of 0.7–2.8 MK, but with a higher probability near the peak sensitivities of the three filters. We conclude that we indeed resolve “elementary” or “monolithic” loop strands with *TRACE*, in terms of isothermal homogeneity. Virtually all earlier studies detected ensembles of multiple strands, while our detected loop strands exhibit much smaller widths ($w \approx 1.4 \pm 0.3$ Mm) and also smaller signal-to-background ratios ($14\% \pm 10\%$). We suggest that the temperature homogeneity of coronal loops up to widths of $w \lesssim 2000$ km is related to their magnetic mapping to photospheric granulation (convection) cells.

Subject headings: Sun: corona — Sun: UV radiation

1. INTRODUCTION

Coronal loops generally consist of multiple strands with different temperatures and densities, which may or may not be resolved in the highest resolution images we have available today, such as from the *Transition Region and Coronal Explorer* (*TRACE*) instrument, which has a pixel size of $0''.5$ (360 km on the solar surface), with a point-spread function FWHM of 2.5 pixels (i.e., $1''.25$ or 910 km), as determined with a blind iterative deconvolution method (Golub et al. 1999; Handy et al. 1999). It is the purpose of this study to analyze the inhomogeneity in temperature and density for a large number of the finest loop structures we can detect with *TRACE*, in order to discriminate whether they are homogeneous elementary strands or inhomogeneous ensembles of unresolved finer strands. This question is of fundamental importance for hydrodynamic modeling of the solar corona (Warren et al. 2002, 2003; Winebarger et al. 2003a, 2003b; Winebarger & Warren 2004; Aschwanden 2004, pp. 67–282). Our strategy is to use the instrument with the highest resolution (i.e., *TRACE*) and the maximum number of temperature filters (i.e., near-simultaneous triple-filter images in 171, 195, and 284 Å, which cover a combined temperature range of $T \approx 0.7$ –2.8 MK).

The spatial structure of coronal loops has become more and more complex with time, since the instrumental resolution of soft X-ray and EUV imagers has been drastically improved over the last decades. The reported width of the finest coronal loops has essentially always been restricted by the spatial resolution of the available instruments, which improved from pixel sizes of $2''.5$ for *Yohkoh* and $2''.6$ for *SOHO* EIT to $0''.5$ for *TRACE*. Besides a high spatial resolution, we also need a broad temperature coverage to disentangle the multistrand composition of coronal loops. Unfortunately, instruments that have been designed to provide a broad temperature coverage, such as *SOHO* CDS, have insufficient spatial resolution to determine the cospatiality of the finest

loop strands in different temperature filter images and thus yield only statistical temperature distributions of ensembles of loop strands. Therefore, the most suitable data sets to disentangle the spatial and thermal composition of coronal loops we have available to date are triple-filter data from *TRACE*, which we use exclusively in this study. There exist only very few loop studies that make use of high-resolution triple-filter images (e.g., Chae et al. [2002] using *TRACE*), but their studies do not quantify the cospatiality of loop structures that are detected in multiple filters. There are studies available that use low-resolution multifilter images (e.g., Schmelz [2002] using *SOHO* CDS with $4''$ pixels, or Schmelz et al. [2003] using *SOHO* EIT with $2''.6$ pixels), which cover a broad temperature range but have a relatively poor spatial resolution and thus cannot address the cospatiality and identity of loop features seen in different temperature filter images. On the theoretical side there exist some modeling efforts with multistrand loop models (e.g., Reale & Peres 2000), but no triple-filter data are fitted therein. Thus, this study represents the first systematic search for elementary (monolithic) loop strands and quantitative analysis of the multistrand structure of coronal loops.

In § 2 we describe the data analysis method, in § 3 we present the statistical results, in § 4 we discuss the implications and consequences, and in § 5 we summarize the conclusions.

2. DATA ANALYSIS METHOD

2.1. Observational Characteristics of Multistrand Loops

We illustrate the concept of multistrand loops and the expected observational characteristics in different temperature filter images in Figure 1. For the sake of simplicity we illustrate the concept only with two filter images (say, 171 and 195 Å), although we use always three filters (171, 195, and 284 Å) in the following analysis. Since we do not know a priori whether we resolve the finest loop strands, we may consider two groups of cases: one

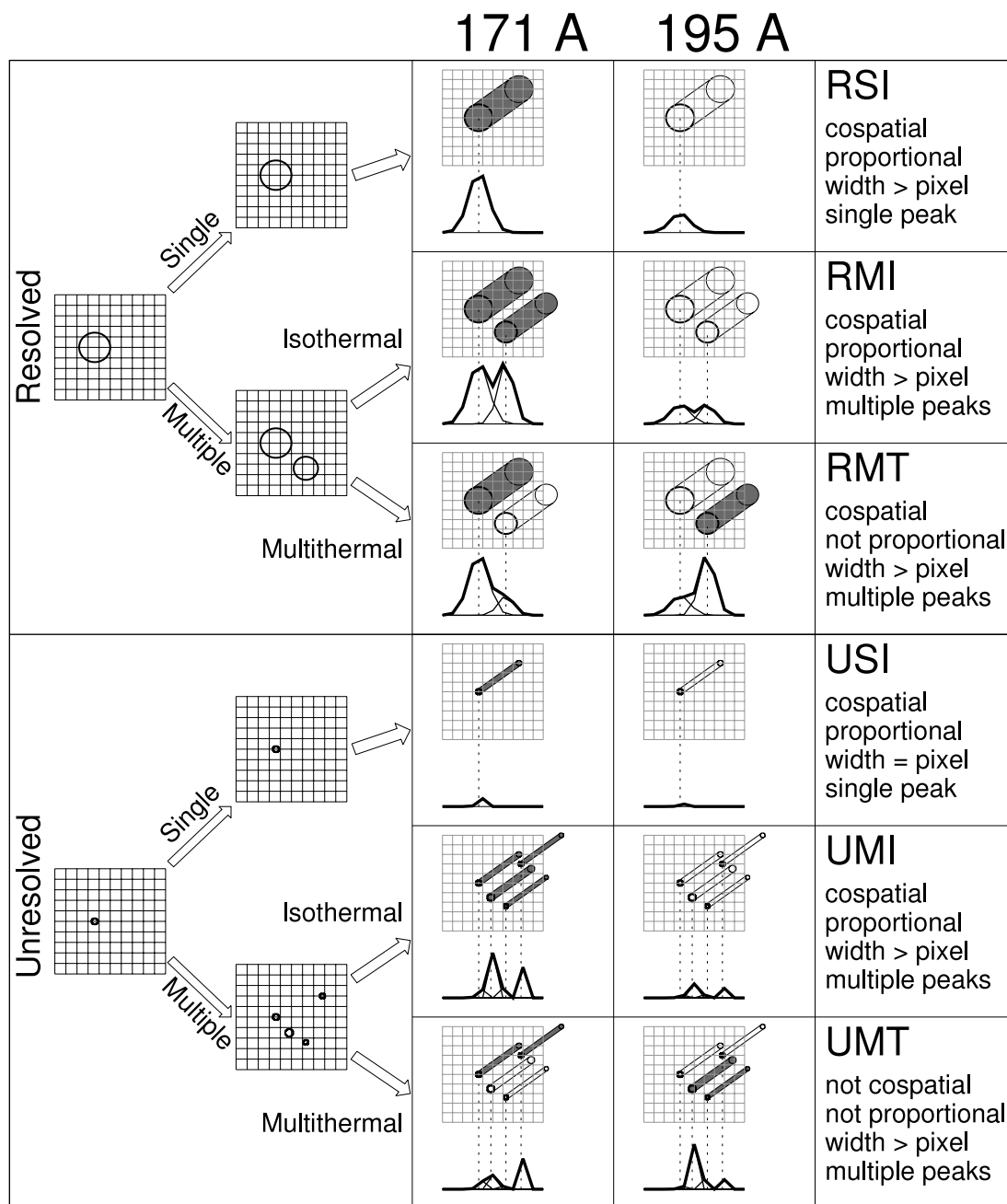


FIG. 1.—Observational signatures of multistrand loops sketched for resolved (R) and unresolved (U) loop strands and further broken down for single (S) and multiple (M) loop strand models, as well as for isothermal (I) and multithermal (T) compositions. The cross sections of loop strands are visualized with circles that have a diameter larger (*top left*) or smaller (*bottom left*) than the pixel size of the image. The cross-sectional flux profiles $f_{171}(x)$ and $f_{195}(x)$ are shown as functions of the position x in perpendicular direction to the loop axis (*right panels*) for two filters, where the gray color indicates that a loop strand has a high emission measure in the corresponding temperature filter, while the white color indicates a low emission measure in the corresponding filter (*right panels*). The six models are labeled RSI, RMI, RMT, USI, UMI, UMT, and the expected observational characteristics are listed on the right-hand side.

group of loop models that consists of resolved (R) loop strands (Fig. 1, *top half*; models RSI, RMI, RMT), and one with unresolved (U) loop strands (Fig. 1, *bottom half*; models USI, UMI, UMT). Further, we might subdivide loop models that consist of either a single (S) strand or multiple (M) strands. In addition, models with multiple loop strands may further be subdivided into isothermal (I) or multithermal (T) compositions.

The single-strand models (RSI and USI) can only be distinguished in the observed loop widths, where unresolved loop strands (model USI) exhibit loop widths corresponding to the instrumental resolution, while resolved loop strands (model RSI) show arbitrarily larger widths. Since single-strand loops have a

single temperature, they should exhibit a cross-sectional loop profile $I(x)$ (in perpendicular direction to the loop axis) with a single peak, which is cospatial in different filters and proportional with a ratio that corresponds to the filter ratio $Q(T) = R_{195}(T)/R_{171}(T)$ of the filter response functions at the given temperature, e.g., $I_{171}(x) = Q(T)I_{195}(x)$.

If we go to multiple loop strands, the cross-sectional loop profiles are only proportional when each loop strand has the same temperature (models RMI and UMI), while they exhibit a different filter ratio for every peak in the case of resolved multiple strands (model RMT) and can have arbitrarily different ratios at each position x for unresolved strands (model UMT).

In summary, given these observational characteristics, we can infer unique information about the multistrand composition of coronal loops from the characteristics (number of peaks, widths of peaks, co-spatiality, proportionality) of their cross-sectional flux profiles in the three different filters, e.g., $f_{171}(x)$, $f_{195}(x)$, and $f_{284}(x)$. In this first study we use only the simplest model with a single strand (models RSI and USI), which we apply to the finest detected structures seen in *TRACE* images by simultaneous forward fitting of the cross-sectional loop profiles in all three temperature filters. With this method we should be able to determine whether the finest observed loop structures are consistent with a single-strand model or not.

2.2. Instrumental Response Function

The instrumental response functions of the three *TRACE* filters are given in Figure 2, shown on a logarithmic (Fig. 2, *bottom panel*) as well as on a linear scale (Fig. 2, *top panel*). We call these three response functions $R_{171}(T)$, $R_{195}(T)$, and $R_{284}(T)$, which are only a function of temperature T and are defined in units of data units (data number per second and pixel; $\text{DN s}^{-1} \text{ pixel}^{-1}$) per emission measure ($\text{EM} = \int n_e^2 dz$) units (cm^{-5}). The peaks of the response functions are $R_{171}(T = 0.95 \text{ MK}) = 1.1 \times 10^{-26} \text{ DN s}^{-1} \text{ pixel}^{-1} \text{ cm}^{-5}$, $R_{195}(T = 1.36 \text{ MK}) = 8.1 \times 10^{-27} \text{ DN s}^{-1} \text{ pixel}^{-1} \text{ cm}^{-5}$, and $R_{284}(T = 2.00 \text{ MK}) = 7.8 \times 10^{-28} \text{ DN s}^{-1} \text{ pixel}^{-1} \text{ cm}^{-5}$. These values correspond to the default calibration currently used (2005 April) in the *TRACE* software, calculated based on coronal elemental abundances (Feldman 1992) and the ionization balance of Arnaud & Raymond (1992). Alternative calibrations of the response function can be seen in the Appendix of Aschwanden et al. (2000c).

The sensitivities of the 195 and 284 Å filters are lower than that of the 171 Å filter, by factors of 0.74 and 0.07, respectively. This has the consequence that the forward fitting is to a lesser degree constrained in the hottest (284 Å) filter than in the cooler filters. We estimate that the sensitive temperature range extends over $T \approx 0.7\text{--}2.8 \text{ MK}$, if we use only temperatures where the nearest filter has more than 50% of its peak sensitivity.

It is also instructive to compare the relative sensitivities of the three different filters at the peak temperatures. For instance, if a loop structure is detected at $T = 0.95 \text{ MK}$, the peak sensitivity of the 171 Å filter, the 195 Å filter will still show 16% of the 171 Å flux, but the 284 Å filter will show only an undetectable amount of 2% (Fig. 2, *bottom panel*). If a loop structure is detected at $T = 1.36 \text{ MK}$, the peak sensitivity of the 195 Å filter, the 171 Å filter will show 43% of the flux, and the 284 Å filter will show an undetectable amount of 3%. However, if a loop is detected at $T = 2.00 \text{ MK}$, the peak sensitivity of the 284 Å filter, the 171 Å filter will show a relatively bright structure with 32%, but the 195 Å filter shows the brightest structure, with 215% of the flux detected in the 284 Å filter. These relative sensitivities determine the relative weighting of the forward fit in the three different filters.

While the filter ratios $R_{195}(T)/R_{171}(T)$ and $R_{284}(T)/R_{195}(T)$ are ambiguous in the full temperature range of $T = 0.7\text{--}2.8 \text{ MK}$, the combination of the two ratios is unique over the whole range. Thus, we expect a unique temperature determination over the whole range of $T = 0.7\text{--}2.8 \text{ MK}$ when using a forward fitting technique that fits simultaneously all three fluxes F_{171} , F_{195} , and F_{284} .

2.3. Observations

We searched the *TRACE* archive during the first 1.5 yr (1998 May–2000 January) of the mission for triple-filter observations

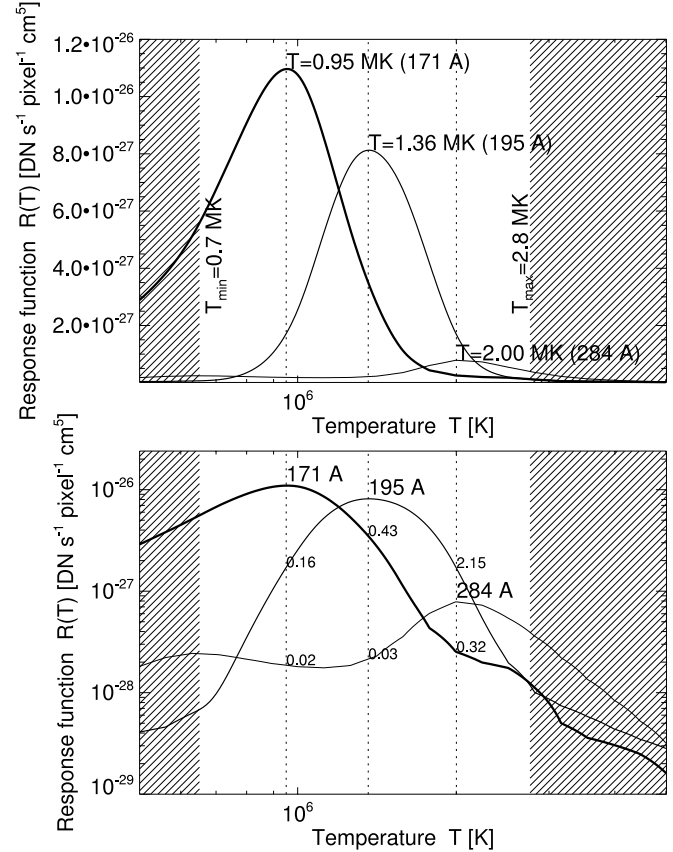


FIG. 2.—Response functions $R_{171}(T)$, $R_{195}(T)$, and $R_{284}(T)$ of the *TRACE* instrument, shown on a linear scale (*top*) and on a logarithmic scale (*bottom*). Also indicated are the peak temperatures (*top*) and sensitivity ratios of the three filters at the peak temperatures (*bottom*).

at the wavelengths of 171, 195, and 284 Å. We found approximately 11,400 near-simultaneous triple-filter image sets, obtained during 61 different days. These dates are listed in Table 1. From those we selected at each day a suitable triple-filter data set near the beginning of each triple-filter observing period, yielding a total of 78 time periods. The starting times of the 171 Å filter images of these 78 analyzed cases are indicated in Table 1. The near-simultaneous 195 and 284 Å images were taken approximately within 1 minute before or after the 171 Å image. The time differences $\Delta t_{195} = t_{195} - t_{171}$ and $\Delta t_{284} = t_{284} - t_{171}$ are given in columns (4) and (5) of Table 1.

The exposure times τ_{171} , τ_{195} , and τ_{284} (Table 1, cols. [6]–[8]) are typically of the order of $\approx 30 \text{ s}$ for the 171 and 195 Å filters and $\approx 60 \text{ s}$ for the less sensitive 284 Å filter. So, although the exposure time is typically doubled for the 284 Å filter, it does not compensate completely for its 14 times lower sensitivity.

The pixel sizes of the 171 and 195 Å images are typically $0''.5$ (yielding a spatial resolution of $1''.25$), while the 284 Å images were almost always taken at a pixel size of $1''.0$ (Table 1, cols. [9]–[11]). We rebinned the 195 and 284 Å images always to the same resolution as the 171 Å images in the data analysis.

The pointing offsets between the images in the three different wavelength filters were determined by the *TRACE* team from image cross-correlations and are listed in columns (12)–(15) of Table 1 (obtained from the differences of the XCEN and YCEN descriptors in the FITS data files). A discrete pointing change occurred after a focus change on 1998 September 25.

Each triple-filter image set was calibrated with the standard *TRACE* software (procedure *TRACE_PREP*) and co-aligned

TABLE 1
TRACE TRIPLE-FILTER DATA SET ANALYZED IN THIS STUDY

NUMBER (1)	DATE (2)	TIME t_{171} (3)	TIME DIFFERENCE ^a (s)		EXPOSURE TIME(s)			PIXEL SIZE(arcsec)			OFFSET ^b			
			Δt_{195} (4)	Δt_{284} (5)	τ_{171} (6)	τ_{195} (7)	τ_{284} (8)	p_{171} (9)	p_{195} (10)	p_{284} (11)	Δx_{195} (12)	Δx_{284} (13)	Δy_{195} (14)	Δy_{284} (15)
0.....	1998 May 13	06:44:35	50	185	38	46	131	0.5	0.5	0.5	0.0	0.0	0.0	0.0
1.....	1998 May 13	07:44:41	32	83	38	27	46	0.5	0.5	0.5	0.0	0.0	0.0	0.0
2.....	1998 May 13	08:38:47	31	167	38	27	131	0.5	0.5	0.5	0.0	0.0	0.0	0.0
3.....	1998 Jun 12	12:05:20	7	24	4	4	13	1.0	1.0	1.0	0.9	1.5	0.7	0.1
4.....	1998 Jun 12	20:00:33	8	34	6	4	23	1.0	1.0	1.0	0.9	1.5	0.7	0.1
5.....	1998 Jun 20	06:01:42	11	31	4	5	16	0.5	0.5	0.5	0.9	1.6	0.7	0.1
6.....	1998 Jun 21	22:43:21	50	275	65	46	220	0.5	0.5	0.5	0.9	1.6	0.7	0.1
7.....	1998 Jun 22	20:38:19	82	217	65	77	131	0.5	0.5	0.5	0.9	1.5	0.7	0.1
8.....	1998 Jul 04	18:16:23	16	40	13	11	19	0.5	0.5	1.0	0.9	1.5	0.7	0.1
9.....	1998 Jul 08	00:17:00	24	42	16	19	13	0.5	0.5	1.0	0.9	1.5	0.7	0.1
10.....	1998 Aug 20	08:43:07	-18	6	13	9	2	0.5	0.5	1.0	0.9	1.5	0.7	0.1
11.....	1998 Aug 22	00:00:14	24	42	16	19	13	0.5	0.5	1.0	0.9	1.5	0.7	0.1
12.....	1998 Nov 02	16:24:43	28	49	16	19	13	0.5	0.5	1.0	0.0	1.0	0.9	0.4
13.....	1998 Nov 21	16:28:00	-44	121	32	38	110	0.5	0.5	1.0	0.0	0.9	0.9	0.5
14.....	1998 Nov 21	18:08:02	-43	122	32	38	110	0.5	0.5	1.0	0.0	1.0	0.9	0.5
15.....	1998 Dec 02	08:17:11	-44	24	32	38	13	0.5	0.5	1.0	0.0	0.9	0.9	0.5
16.....	1998 Dec 12	08:07:25	-44	67	32	38	55	0.5	0.5	1.0	0.0	1.0	0.9	0.4
17.....	1998 Dec 12	10:26:32	-44	66	32	38	55	0.5	0.5	1.0	0.0	1.0	0.9	0.5
18.....	1998 Dec 12	12:03:01	-44	66	32	38	55	0.5	0.5	1.0	0.0	0.9	0.9	0.5
19.....	1998 Dec 12	20:04:14	-44	66	32	38	55	0.5	0.5	1.0	0.0	1.0	0.9	0.5
20.....	1998 Dec 25	12:20:41	-44	67	32	38	55	0.5	0.5	1.0	0.0	0.9	0.9	0.5
21.....	1998 Dec 30	02:23:29	-44	67	32	38	55	0.5	0.5	1.0	0.0	0.9	0.9	0.5
22.....	1999 Jan 31	02:43:57	-44	66	32	38	55	0.5	0.5	1.0	0.0	1.0	0.9	0.5
23.....	1999 Jan 31	06:06:23	-43	67	32	38	55	0.5	0.5	1.0	0.0	1.0	0.9	0.5
24.....	1999 Jan 31	20:14:42	-44	66	32	38	55	0.5	0.5	1.0	0.0	0.9	0.9	0.5
25.....	1999 Jul 11	02:23:24	27	-24	19	23	65	0.5	0.5	0.5	0.0	1.0	0.9	0.5
26.....	1999 Jul 12	01:57:09	-44	67	32	38	55	0.5	0.5	1.0	0.0	1.0	0.9	0.5
27.....	1999 Jul 27	04:08:38	-44	66	32	38	55	0.5	0.5	1.0	0.0	1.0	0.9	0.5
28.....	1999 Jul 27	04:16:19	-44	66	32	38	55	0.5	0.5	1.0	0.0	1.0	0.9	0.5
29.....	1999 Jul 27	04:43:08	-44	66	32	38	55	0.5	0.5	1.0	0.0	1.0	0.9	0.5
30.....	1999 Jul 28	04:27:34	-44	66	32	38	55	0.5	0.5	1.0	0.0	1.0	0.9	0.5
31.....	1999 Jul 29	07:23:52	-44	67	32	38	55	0.5	0.5	1.0	0.0	1.0	0.9	0.5
32.....	1999 Jul 30	04:16:52	-44	66	32	38	55	0.5	0.5	1.0	0.0	0.9	0.9	0.5
33.....	1999 Jul 31	05:17:21	-44	66	32	38	55	0.5	0.5	1.0	0.0	1.0	0.9	0.4
34.....	1999 Aug 01	05:01:40	-44	66	32	38	55	0.5	0.5	1.0	0.0	0.9	0.9	0.4
35.....	1999 Aug 08	04:01:28	-44	124	32	38	55	0.5	0.5	1.0	0.0	1.0	0.9	0.5
36.....	1999 Aug 08	16:22:58	18	70	11	13	16	0.5	0.5	1.0	0.0	1.0	0.9	0.5
37.....	1999 Aug 09	13:26:34	18	-22	19	13	16	0.5	0.5	1.0	0.0	1.0	0.9	0.5
38.....	1999 Aug 09	16:30:41	18	-22	19	13	16	0.5	0.5	1.0	0.0	1.0	0.9	0.5
39.....	1999 Aug 09	19:35:29	18	-22	19	13	16	0.5	0.5	1.0	0.0	1.0	0.9	0.5
40.....	1999 Aug 09	22:15:02	18	-23	19	13	16	0.5	0.5	1.0	0.0	1.0	0.9	0.5
41.....	1999 Aug 10	00:47:18	-37	51	32	23	46	0.5	0.5	1.0	0.0	1.0	0.9	0.4
42.....	1999 Aug 11	10:12:39	-24	20	19	13	16	0.5	0.5	1.0	0.0	1.0	0.9	0.5
43.....	1999 Aug 12	02:12:01	-44	66	32	38	55	0.5	0.5	1.0	0.0	1.0	0.9	0.4
44.....	1999 Aug 13	00:07:24	-44	66	32	38	55	0.5	0.5	1.0	0.0	0.9	0.9	0.5
45.....	1999 Aug 15	04:31:43	-44	66	32	38	55	0.5	0.5	1.0	0.0	1.0	0.9	0.5
46.....	1999 Aug 17	00:17:24	-44	66	32	38	55	0.5	0.5	1.0	0.0	1.0	0.9	0.5
47.....	1999 Aug 18	00:03:23	70	-23	19	65	5	0.5	0.5	1.0	0.0	0.9	0.9	0.5
48.....	1999 Aug 19	01:42:10	-44	66	32	38	55	0.5	0.5	1.0	0.0	1.0	0.9	0.5
49.....	1999 Aug 20	04:20:14	-44	66	32	38	55	0.5	0.5	1.0	0.0	0.9	0.9	0.5
50.....	1999 Aug 21	04:29:18	-44	66	32	38	55	0.5	0.5	1.0	0.0	0.9	0.9	0.5
51.....	1999 Aug 22	03:04:52	-24	18	16	11	13	0.5	0.5	1.0	0.0	0.9	0.9	0.5
52.....	1999 Aug 23	01:08:31	-43	67	32	38	55	0.5	0.5	1.0	0.0	0.9	0.9	0.4
53.....	1999 Aug 24	01:26:21	-44	66	32	38	55	0.5	0.5	1.0	0.0	0.9	0.9	0.4
54.....	1999 Aug 25	01:37:29	-44	67	32	38	55	0.5	0.5	1.0	0.0	1.0	0.9	0.5
55.....	1999 Aug 26	01:03:25	-27	20	19	4	16	0.5	0.5	1.0	0.0	1.0	0.9	0.5
56.....	1999 Aug 27	00:18:23	-44	67	32	38	55	0.5	0.5	1.0	0.0	1.0	0.9	0.5
57.....	1999 Aug 28	00:22:55	-44	67	32	38	55	0.5	0.5	1.0	0.0	1.0	0.9	0.5
58.....	1999 Sep 12	00:45:22	-28	67	16	19	55	0.5	0.5	0.5	0.0	1.0	0.9	0.5
59.....	1999 Sep 15	00:19:37	-44	66	32	38	55	0.5	0.5	1.0	0.0	1.0	0.9	0.5
60.....	1999 Sep 30	00:45:34	-44	66	32	38	55	0.5	0.5	1.0	0.0	1.0	0.9	0.5

TABLE 1—*Continued*

NUMBER (1)	DATE (2)	TIME t_{171} (3)	TIME DIFFERENCE ^a (s)		EXPOSURE TIME (s)			PIXEL SIZE (arcsec)			OFFSET ^b			
			Δt_{195} (4)	Δt_{284} (5)	τ_{171} (6)	τ_{195} (7)	τ_{284} (8)	p_{171} (9)	p_{195} (10)	p_{284} (11)	Δx_{195} (12)	Δx_{284} (13)	Δy_{195} (14)	Δy_{284} (15)
61.....	1999 Oct 07	07:20:12	-110	-44	32	38	55	0.5	0.5	0.5	0.0	0.9	0.9	0.5
62.....	1999 Oct 21	08:15:17	-36	-22	19	8	9	0.5	0.5	1.0	0.0	1.0	0.9	0.5
63.....	1999 Oct 29	12:25:26	-36	-22	19	13	9	0.5	0.5	1.0	0.0	1.0	0.9	0.5
64.....	1999 Nov 06	02:21:13	-28	-14	11	13	9	0.5	0.5	1.0	0.0	1.0	0.9	0.5
65.....	1999 Nov 06	02:52:40	-36	-15	11	13	16	0.5	0.5	1.0	0.0	1.0	0.9	0.5
66.....	1999 Nov 06	04:22:59	-35	-14	11	13	16	0.5	0.5	1.0	0.0	1.0	0.9	0.5
67.....	1999 Nov 10	00:13:01	-29	67	16	19	55	0.5	0.5	0.5	0.0	1.0	0.9	0.5
68.....	1999 Nov 12	06:21:18	-24	-10	6	19	9	0.5	0.5	1.0	0.0	0.9	0.9	0.5
69.....	1999 Nov 14	01:13:05	-28	-14	11	13	9	0.5	0.5	1.0	0.0	0.9	0.9	0.5
70.....	1999 Dec 06	00:38:12	-107	-41	32	38	55	0.5	0.5	1.0	0.0	1.0	0.9	0.5
71.....	1999 Dec 16	01:31:51	-107	-41	32	38	55	0.5	0.5	1.0	0.0	1.0	0.9	0.5
72.....	1999 Dec 23	01:42:44	-107	-40	32	38	55	0.5	0.5	1.0	0.0	1.0	0.9	0.5
73.....	1999 Dec 26	04:26:29	-54	-22	19	23	27	0.5	0.5	1.0	0.0	0.9	0.9	0.5
74.....	1999 Dec 28	06:09:29	-43	-22	19	23	16	0.5	0.5	1.0	0.0	0.9	0.9	0.4
75.....	2000 Jan 06	06:48:36	-28	-14	11	13	9	0.5	0.5	1.0	0.0	1.0	0.9	0.4
76.....	2000 Jan 08	00:06:29	-54	-22	19	23	27	0.5	0.5	1.0	0.0	1.0	0.9	0.5
77.....	2000 Jan 11	04:59:51	-67	-35	32	13	27	0.5	0.5	1.0	0.0	0.9	0.9	0.5

^a Time difference of 195 and 284 Å filters with respect to 171 Å.

^b Offset of image pointing (XCEN, YCEN) of 195 and 284 Å filters with respect to 171 Å.

according to the pointing offsets (using the keyword /wave2point in the procedure TRACE_PREP).

2.4. Selection of Loops

Several hundred coronal loops can usually be discerned in every triple-filter image set. However, most of the loop structures occur in active regions where they appear in highly nested configurations and are difficult to disentangle from the loops in the foreground and background and from moss structure in the transition region. The confusion is most severe for coronal loops outside of the limb. The most suitable cases for our analysis are loops that appear isolated, have a high contrast to the background, and have a simple-structured background. Moreover, since we are interested in the finest loop strand structures, we focus on relatively thin loops. Furthermore, we wish to have comprehensive temperature coverage and thus search in all three temperature filters. So, our loop selection criteria are (1) thin loops, (2) high-contrast loops with good signal-to-background ratio, (3) spatially isolated loops if possible, (4) simple-structured background, and (5) unbiased selection of temperatures. To fulfill the last criterion as well as possible, we select for each triple-filter set one loop in each temperature filter. However, often there is no suitable loop present in the least sensitive 284 Å filter, and thus we end up with a much higher number of selected loops in the 171 Å filter.

In order to localize thin loops, we apply a high-pass filter with a boxcar function of $N_{\text{smooth}} = 7$; i.e., we subtract the boxcar-smoothed image from the original image, a method also known as unsharp masking. Such a high-pass filter method has the advantage that a fine structure can be easily traced even when embedded in a sloping background but introduces the bias that only structures with widths smaller than the boxcar can be detected. Since our boxcar is 7 pixels, we expect detection of loop widths between 1 (0.5 or 350 km) and 7 pixels (3.5 or 2540 km). The highest contrast is expected for features with a mean width of 4 pixels (2.0 or 1450 km). We will see that the observed distribution of loop widths closely follows these expectations.

From each of the 78 triple-filter image data sets we select three different loops for analysis, totaling to a sample of 234 coronal loop structures. Often it is not possible to trace complete loops,

so many of the structures represent half loops, partial segments of loops, or segments of open field lines. However, since we are only interested in the physical parameters of loop cross sections, it does not matter whether the analyzed structures represent incomplete loops or what segment they are part of.

2.5. Measurement of Loop Parameters

A selected loop is traced at 10 positions along its length in the filter image where it is best visible from a high-pass filtered, enlarged visual display. This yields 10 image coordinate positions ($X_i, Y_i, i = 1, \dots, 10$). These 10 spline points are then interpolated with a two-dimensional spline function, which yields a total of 80 loop coordinates ($X_i, Y_i, i = 1, \dots, 80$) along the curved loop axis. For each of these 80 central loop positions, the image fluxes are interpolated along a perpendicular direction x to the loop axis by bilinear interpolation, typically over a length of $n_x = 10$ pixels (5.0 or 3620 km). This yields three cospatial cross-sectional loop flux profiles $F_{171}(x_j), F_{195}(x_j), F_{284}(x_j), j = 1, \dots, n_x$ for each loop length position ($X_i, Y_i, i = 1, \dots, 80$), in units of data numbers per second (DN s⁻¹), which can be fitted with a theoretical model. So, all in all we extracted from 78 triple-filter data sets a total of $78 \times 3 = 234$ loops and $78 \times 3 \times 80 = 18,720$ loop positions, each one providing $3 \times n_x = 30$ data points, totaling to 561,600 data points for model fitting.

2.6. Parameterization of Single-Strand Model

The simplest single-strand model has to quantify at least the geometric cross section at an arbitrary temperature and some background model for each filter. We parameterize the geometric one-dimensional loop cross section with a Gaussian function, which requires three free parameters (peak value, peak position, and Gaussian width). In terms of a physical model it is most suitable to express the peak value with the emission measure $EM = n_e^2 w$, where the FWHM w relates to the Gaussian width σ_w by $w = 2\sigma_w(2 \ln 2)^{1/2} = 2.35\sigma_w$. The temperature distribution is in the simplest way characterized by a single temperature T (isothermal model) or by a differential emission measure distribution $DEM(T)/dT$ (multithermal model). So, the minimum

number of free parameters is four in the simplest case of an isothermal loop structure (the emission measure EM, the peak position x_0 , the Gaussian width σ_w , and the temperature T) and arbitrarily higher for a multithermal model.

In addition, we need to specify a background, which can be arbitrarily different in each of the three filters. A constant background flux for each filter is not amenable because loops are often found on a sloped background. We need therefore to specify the background at least to first order, which is a linear function with two free parameters, amounting to six free parameters for three filters. Thus, our minimal model contains 10 free parameters: 4 for an (isothermal) loop structure and 6 for the background. The fact that we fit the same Gaussian function of the loop cross section profile in each filter reinforces that we fit only cospatial structures in the three filters. Denoting the background flux constant with b and the gradient with db , the linear background profile $b(x)$ in each filter is

$$\begin{aligned} b_{171}(x) &= b_1 + db_1 x, \\ b_{195}(x) &= b_2 + db_2 x, \\ b_{284}(x) &= b_3 + db_3 x. \end{aligned} \quad (1)$$

Multithermal model.—For an unconstrained multithermal model we can specify the differential emission measure distribution, which in the simplest case can be characterized by three different emission measures (EM_1 , EM_2 , and EM_3) at the peak sensitivities (R_1 , R_2 , and R_3) of the three filters,

$$\begin{aligned} f_{171}(x) &= EM_1 \exp \left[-\frac{(x - x_0)^2}{2\sigma_w^2} \right] R_1, \\ f_{195}(x) &= EM_2 \exp \left[-\frac{(x - x_0)^2}{2\sigma_w^2} \right] R_2, \\ f_{284}(x) &= EM_3 \exp \left[-\frac{(x - x_0)^2}{2\sigma_w^2} \right] R_3, \end{aligned} \quad (2)$$

which occur at $R_1 = R_{171}(T \approx 0.95 \text{ MK})$, $R_2 = R_{195}(T \approx 1.36 \text{ MK})$, and $R_3 = R_{284}(T \approx 2.00 \text{ MK})$ (see § 2.2). Strictly speaking, the EM_i parameters are a shorthand for $EM_i = \int [dEM(T)/dT] [R(T)/R_i] dT$ in terms of a standard multithermal DEM distribution $dEM(T)/dT$. So, our minimum-parameter multithermal model contains the following 11 free parameters: EM_1 , EM_2 , EM_3 , x_0 , σ_w , b_1 , db_1 , b_2 , db_2 , b_3 , and db_3 .

Isothermal model.—The isothermal model is a special case of the general multithermal model. While the three flux values ($f_1 = EM_1 R_1$, $f_2 = EM_2 R_2$, $f_3 = EM_3 R_3$) are independently fitted in our multithermal model, the isothermal model is equivalent to a DEM distribution that is collapsed to a δ -function with a single emission measure value EM at a single temperature T . Therefore, the fluxes in the three filters are not independent, but defined by the filter response functions $R_{\text{filter}}(T)$ at the (single) temperature T ,

$$\begin{aligned} f_{171}(x) &= EM \exp \left[-\frac{(x - x_0)^2}{2\sigma_w^2} \right] R_{171}(T), \\ f_{195}(x) &= EM \exp \left[-\frac{(x - x_0)^2}{2\sigma_w^2} \right] R_{195}(T), \\ f_{284}(x) &= EM \exp \left[-\frac{(x - x_0)^2}{2\sigma_w^2} \right] R_{284}(T). \end{aligned} \quad (3)$$

So, our minimum-parameter isothermal model contains the following 10 free parameters: EM, T , x_0 , σ_w , b_1 , db_1 , b_2 , db_2 , b_3 , and db_3 .

The theoretical model of the three loop profiles consists then of the superposition of the background flux $b(x)$ and the loop flux $f(x)$,

$$f(x) = [f_{171}(x) + b_{171}(x), f_{195}(x) + b_{195}(x), f_{284}(x) + b_{284}(x)]. \quad (4)$$

2.7. Forward Fitting of Single-Strand Model

To fit the theoretical triple-filter flux profiles $f(x)$ to the observed profiles $f^{\text{obs}}(x)$, we have to convert the fluxes (in units DN s^{-1}) into counts N , so that we can apply Poisson statistics in a least- χ^2 test.

Each detected photon produces an electron in the CCD silicon pixel, which is amplified and produces an analog-to-digital converter (ADC) readout with a conversion factor of $q_{\text{DN}} = 12$ electrons DN^{-1} (Handy et al. 1999).

An additional subtle effect that has to be considered to obtain the correct Poisson statistics is the bilinear interpolation we used in interpolating the fluxes at a curved array grid. Because bilinear interpolation in a Cartesian grid is equivalent to the weighted average of the four nearest neighbors, the count statistics is boosted by factors of $1 \leq N_{\text{bi}} \leq 4$, depending on how close the interpolated position is located to the next neighbors. If the interpolated position coincides with a Cartesian grid point, it uses $N_{\text{bi}} = 1$ pixel values; if the position is between two grid points, it uses $N_{\text{bi}} = 2$ pixel values; and if it is in between two grid points in both the x - and y -direction, it uses $N_{\text{bi}} = 4$ pixel values. In order to estimate the average number of pixels used in a bilinear interpolation scheme, we can average the number of nearest neighbors used in a coincident Cartesian grid with the double resolution, which is $\langle N_{\text{bi}} \rangle = (1 + 2 + 2 + 4)/4 = 9/4 = 2.25$.

Since the exposure times τ_{filt} are different for each filter (Table 1, cols. [6]–[8]), we have to multiply the fluxes in each filter separately to obtain the counts. Thus, the photon or electron counts (used for Poisson statistics) of the observed cross-sectional profiles are

$$N^{\text{obs}}(x) = [f_{171}^{\text{obs}}(x)\tau_{171}, f_{195}^{\text{obs}}(x)\tau_{195}, f_{284}^{\text{obs}}(x)\tau_{284}] N_{\text{bi}} q_{\text{DN}}. \quad (5)$$

The theoretical profile in units of counts $N(x)$ is correspondingly

$$N(x) = [\{f_{171}(x) + b_{171}(x)\}\tau_{171}, \{f_{195}(x) + b_{195}(x)\}\tau_{195}, \{f_{284}(x) + b_{284}(x)\}\tau_{284}] N_{\text{bi}} q_{\text{DN}}. \quad (6)$$

We assess the goodness of the fit with the standard χ^2 test,

$$\chi^2 = \sum_{i=1}^n \frac{[N(x) - N^{\text{obs}}(x)]^2}{\sigma(x)^2}, \quad (7)$$

where the standard deviation σ is defined from the Poisson statistics

$$\sigma(x) = \sqrt{N^{\text{obs}}(x)} \quad (8)$$

and the reduced χ^2 is defined by

$$\chi_{\text{red}}^2 = \frac{\chi^2}{(n - n_{\text{free}})}, \quad (9)$$

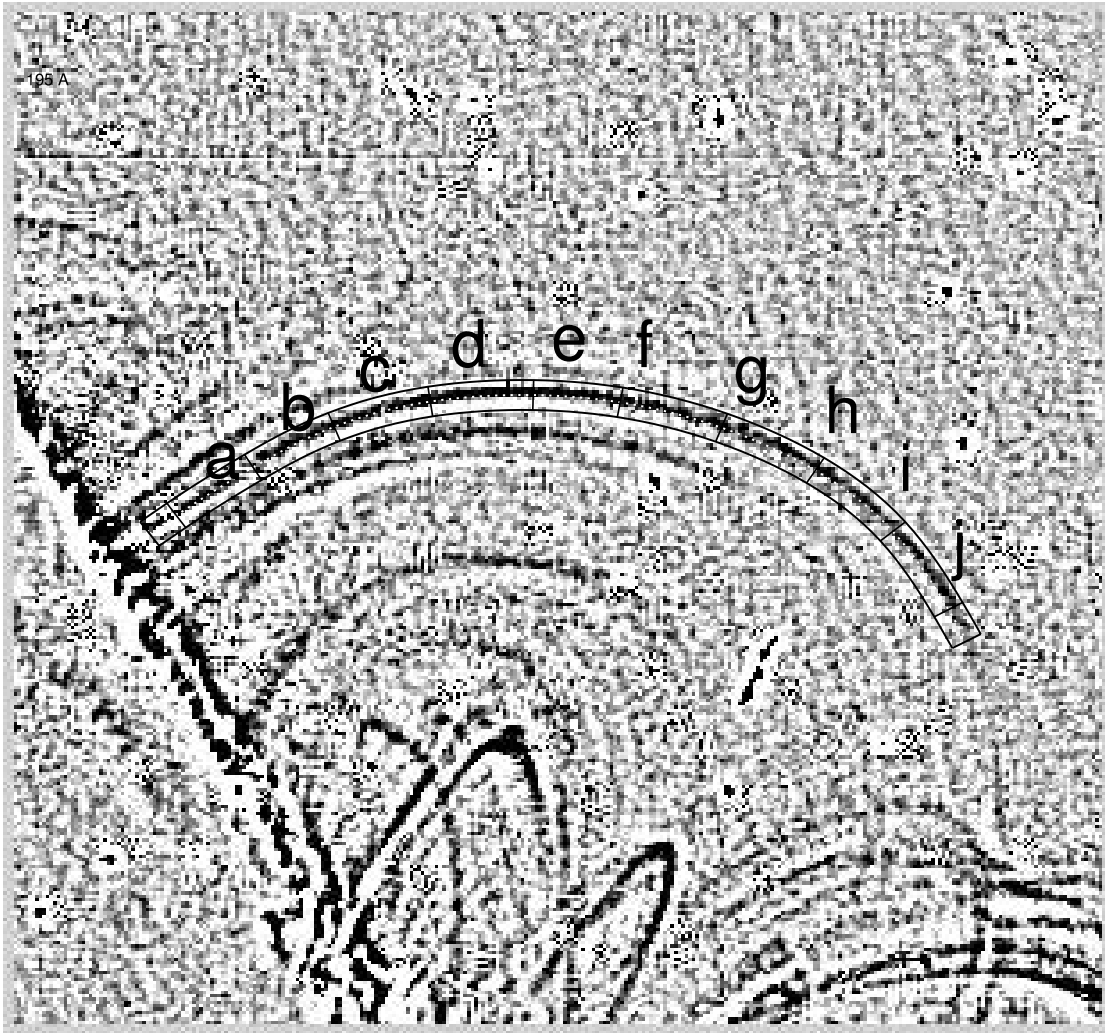


FIG. 3.—High-pass filtered image, recorded by *TRACE* on 1999 August 09, 19:35:29 UT, at 171 Å, extracted in the pixel range [406:716, 653:963] from the original 1024 × 1024 image. The high-pass filtered image is generated by subtracting a (7 pixel wide) boxcar-smoothed image from the original image. The pixel size is 0.5. A particular, little-confused loop segment (39A) is traced and marked with a stripe, and 10 positions *a–j* are marked, which correspond to the positions $s/L = 0.05, 0.15, 0.25, \dots, 0.95$, for which the cross-sectional flux profiles are shown in Fig. 4. Cosmic-ray spikes or particle hits are noticeable in this image in areas where 8 × 8 pixel blocks show nonrandom patterns from the JPEG compression.

with $n = 3 \times n_x = 30$ the number of data points per triple-filter profile and n_{free} the number of free parameters of the theoretical model, which is $n_{\text{free}} = 10$ for the isothermal model and $n_{\text{free}} = 11$ for the multithermal model. The reduced χ^2 has an expectation value of unity. For the numerical values we quote the square root of the reduced χ^2 in this study, i.e., $\chi_{\text{red}} = (\chi_{\text{red}}^2)^{1/2}$, which directly quantifies the goodness of fit in units of standard deviations.

3. RESULTS

3.1. Example of an Analyzed Cool Loop

An example of such a forward fitting procedure (using the isothermal model) is given in Figures 3, 4, and 5 for case 39A (one of the three loops analyzed from triple-filter data set 39 in Table 1). From the original triple-filter images in 171, 195, and 284 Å (with image sizes of 1024 × 1024 pixels), a subimage in the pixel range of [406:716, 653:963] has been extracted in each filter. These subimages have been high-pass filtered with a boxcar of 7 pixels. In an enlarged version of the high-pass filtered 195 Å subimage, a half-loop structure has been marked and extracted as a stripe with a width of $n_x = 10$ pixels (indicated as a curved stripe in Fig. 3).

The original and the high-pass filtered subimages of all three filters are shown in Figure 4 (*first and second columns on the left*), with the loop stripe indicated. From the 80 cross-sectional loop profiles, a subset of 10 are shown at the positions $s/L = 0.05, 0.15, \dots, 0.95$ in the third, fourth, and fifth columns of Figure 4, including error bars of the count statistics and fits of the linear background and Gaussian loop shape. Note that the flux enhancement (i.e., the signal-to-background ratio) is only $\approx 20\%$ of the background flux. An enlarged view of the cross-sectional profiles with the linear background subtracted is shown in the sixth, seventh, and eighth columns of Figure 4. Note that the loop is about equally bright in the 171 and 195 Å filters, while the 284 Å filter essentially shows only noise or faint loop structures from the background above the limb. The simultaneous fit in all three filters reinforces that only cospatial loop structures are fitted, which can be verified from the coincidence of the peaks within about 1 pixel near the loop axis, in both the 171 and 195 Å cross-sectional profiles shown in rows 6–8 of Figure 4. The reduced χ^2 are also indicated in row 6, which are $\chi^2 = 2.91, 2.54, 1.31, \dots, 1.65$ at the 10 indicated positions. The background-subtracted peak fluxes in the three filters are also shown in the rightmost column of Figure 4, with the best-fit temperatures indicated, which are

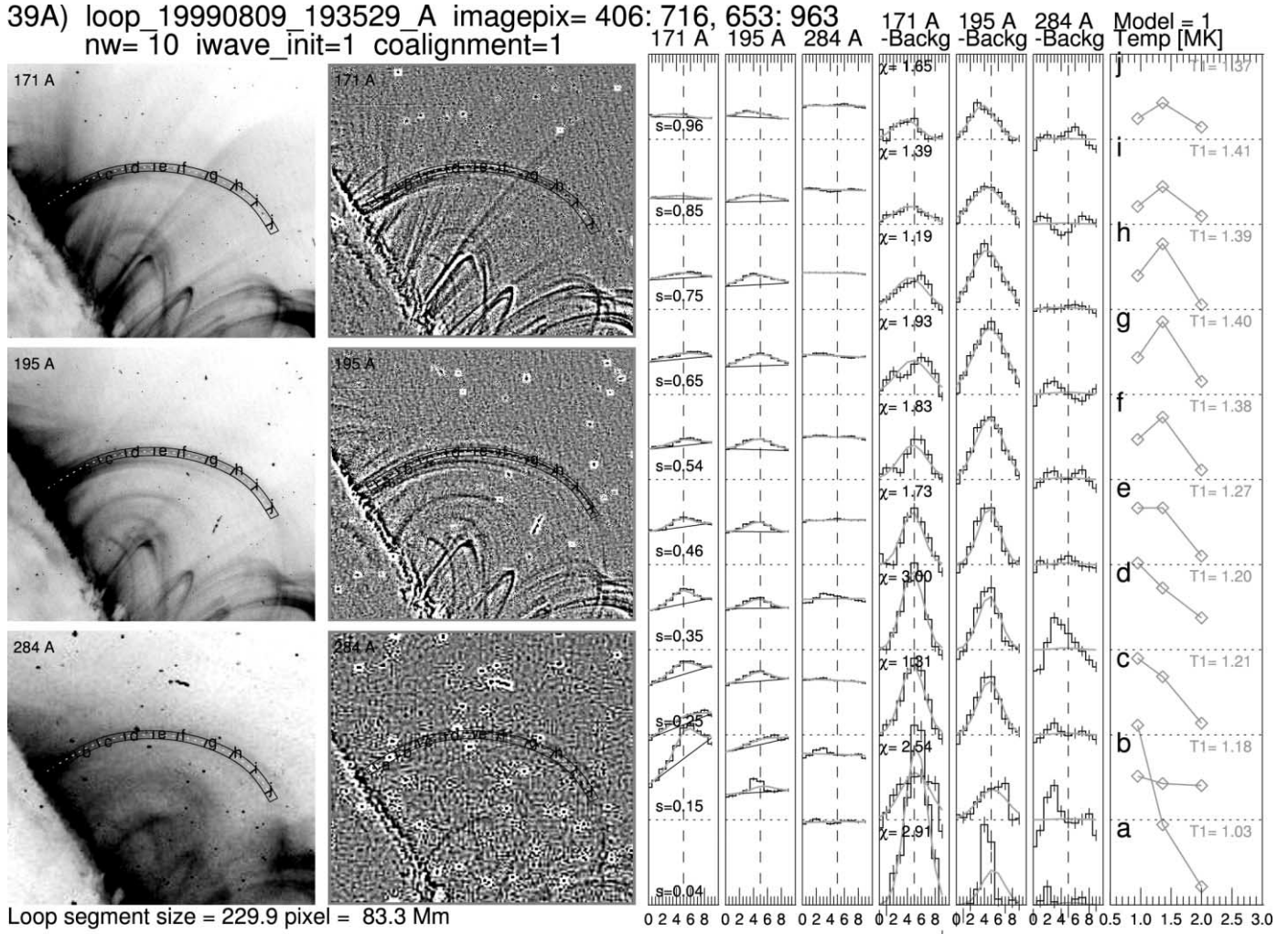


FIG. 4.—Example of data analysis for loop 39A, selected in Fig. 3: the extracted original images in 171 Å (top left), 195 Å (middle left), and 284 Å (bottom left), the high-pass filtered images (second column), the cross-sectional flux profiles at 10 loop positions in 171 Å (third column), 195 Å (fourth column), and 284 Å (fifth column), along with the best fits of the background (linear function) and loop (Gaussian function), the corresponding background-subtracted profiles with error bars and χ^2 values of the fit (sixth, seventh, and eighth columns), and the loop-associated fluxes as a function of temperature (right column), along with the best-fit single-temperature value. See § 3.1 for descriptions and Fig. 5 for physical parameters as a function of loop length.

$T = 1.03, 1.18, 1.21, \dots, 1.37$ MK at the 10 indicated positions. This is a fairly typical case, where confusion by crossing background loops affects the fits at some cross-sectional positions.

A run of the best-fit parameters at the 80 positions s along the loop from Figure 4 is explicitly shown in Figure 5. The fraction of acceptable fits is marked by diamonds in Figure 5, which have to be within the range of $\chi_{\text{red}} \leq 1.5$. A total of 22 out of the 80 loop positions (28%) fulfill the criteria for acceptable fits. The mean and standard deviations indicated in Figure 5 refer only to those 22 acceptable fits. The temperature starts at $T(s=0) \approx 1.00$ MK at the loop footpoint and rises to $T(s=L) \approx 1.3$ MK at the looptop, with a mean and standard deviation of $T = 1.34 \pm 0.12$ MK. The centroid loop position is $x_0 = -210 \pm 190$ km with respect to the selected trajectory that has been visually defined and interpolated with a two-dimensional spline curve in Figure 3. The Gaussian widths of the loop are $\sigma_w = 690 \pm 120$ km, which translates into an FWHM of $w = 2.35\sigma_w = 1620 \pm 280$ km (Fig. 5, middle right panel). The emission measure has a logarithmic mean of $\log \text{EM} = 26.30 \pm 0.14$ (with the EM in units of cm^{-5} ; Fig. 5, middle left panel). Assuming that the loop has a circular cross section, so that we can approximate the line-of-sight depth z of the loop with its transverse cross section w , i.e.,

$z \approx w$, and assuming a filling factor of unity in the corona, we can then deduce an electron density from $n_e = (\text{EM}/z)^{1/2}$. For loop 39A we find $\log n_e = 9.05 \pm 0.08$ or a mean density of $n_e = 1.1 \times 10^9 \text{ cm}^{-3}$. The density decreases slightly with distance from the footpoint (which is here increasing altitude), as expected for gravitational stratification (see the limb at the bottom left corner of Fig. 3). The χ^2 values scatter mostly in the range of 1.0–2.5 (Fig. 5, bottom right panel). The fitted functions and error bars are explicitly shown in Figure 4 for a subset of 10 positions, which reveal that contaminations from background structures in the primary filters (171 and 195 Å) that are sensitive to the selected loop and even more so in secondary filters (i.e., the 284 Å here) give rise to higher χ^2 values than expected for best fits ($\chi^2 \approx 1$). The best fit among the subset shown in Figure 4 is at position h (i.e., $s/L = 0.75$) with $\chi_{\text{red}} = 1.19$.

3.2. Example of an Analyzed Hot Loop

A second example is shown in Figure 6, for case 3C (one of the three loops analyzed from the triple-filter data set 3 in Table 1). While the example of a cool loop (case 39A shown in Figs. 3–5) shows loop-associated emission dominantly in the 171 and 195 Å

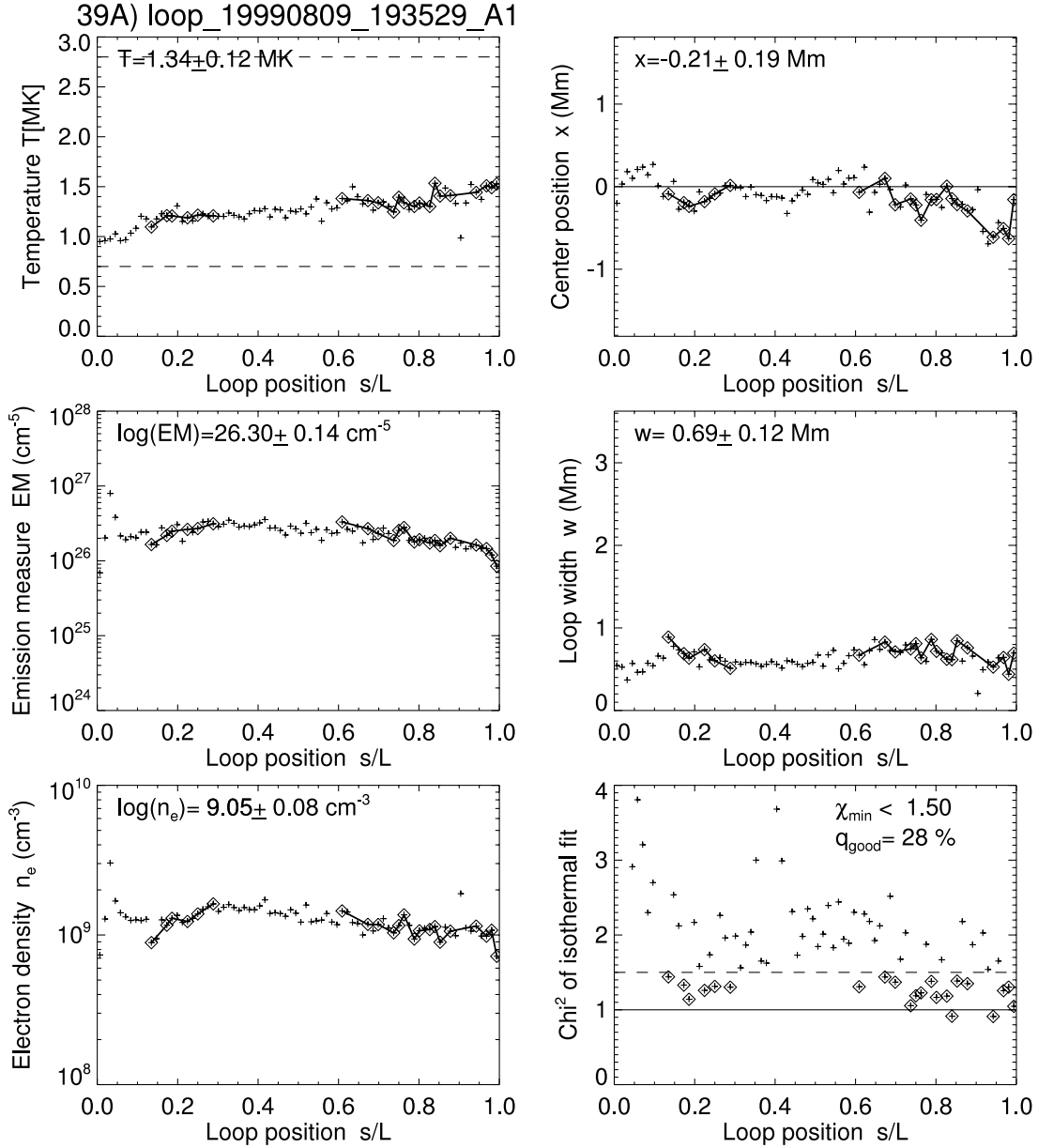


FIG. 5.—Runs of best-fit values of electron temperature $T(s)$ (top left), emission measure $EM(s)$ (middle left), electron density $n_e(s)$ (bottom left), loop center position $x_0(s)$ (top right), loop width $w(s)$ (middle right), and goodness of fit $\chi^2(s)$ (bottom right) as a function of the normalized loop position $0 < s/L < 1$. The mean values and standard deviations of acceptable fits are given in each frame. A fraction of 28% of the fits from the 80 loop positions represent acceptable fits with $\chi_{\text{red}} \leq 1.5$. These parameters refer to the same loop pictured in Figs. 3 and 4.

filters, the hot loop 3C shows loop-associated emission dominantly in the 195 and 284 Å filters, while almost no spatially correlated emission is seen in the 171 Å filter in the upper part of the loop. Note also that the EUV emission is noisier than in case 39A because shorter exposure times have been used. The fitted loop cross sections have best-fit temperatures of $T = 1.24, 1.29, 1.40, \dots, 1.70$ MK at the 10 loop positions ($s/L = 0.05, 0.15, 0.25, \dots, 0.95$) indicated in Figure 6, and the reduced χ^2 values are $\chi_{\text{red}} = 1.95, 2.40, 2.33, \dots, 1.30$ at the corresponding positions. The uncontaminated loop positions have χ^2 values in the range of $\chi_{\text{red}} \leq 1.5$.

Acceptable fits (with $\chi_{\text{red}} \leq 1.5$) are mostly found in the upper part of the loop. Statistical values are the temperature with a mean of $T = 1.84 \pm 0.04$ MK, the emission measure with $\log EM = 26.94 \pm 0.12$ cm $^{-5}$, the electron density with $n_e = 9.26 \pm 0.06$ cm $^{-3}$, the centroid position with $x_0 = 0.37 \pm 0.37$ Mm, the

Gaussian width with $\sigma_w = 1.12 \pm 0.13$ Mm, and the goodness of fit with $0.7 \lesssim \chi_{\text{red}} \lesssim 2.5$. The best fit among the subset shown in Figure 6 is at position *g* (i.e., $s/L = 0.65$) with $\chi_{\text{red}} = 0.86$. Only 37% of the loop positions show an acceptable fit. However, these data represent the noisiest analyzed case (with only 4 s exposure time in the 171 and 195 Å filters and 13 s in the 284 Å filter; see Table 1).

Anyway, the two examples shown in Figures 3–6 demonstrate that our forward fitting method (using the isothermal model) with triple-filter images allows unambiguous temperature determinations over the range from $\lesssim 1.0$ to $\gtrsim 2.0$ MK at least, yielding relatively consistent temperature profiles $T(s)$ along the loops. The same data analysis procedure described for these two examples 39A and 3C has been carried out for all 234 selected loops, labeled with the numbers 0, \dots , 77 (in Table 1) and the letters A, B, C for three loops selected from each of the 78 triple-filter data sets.

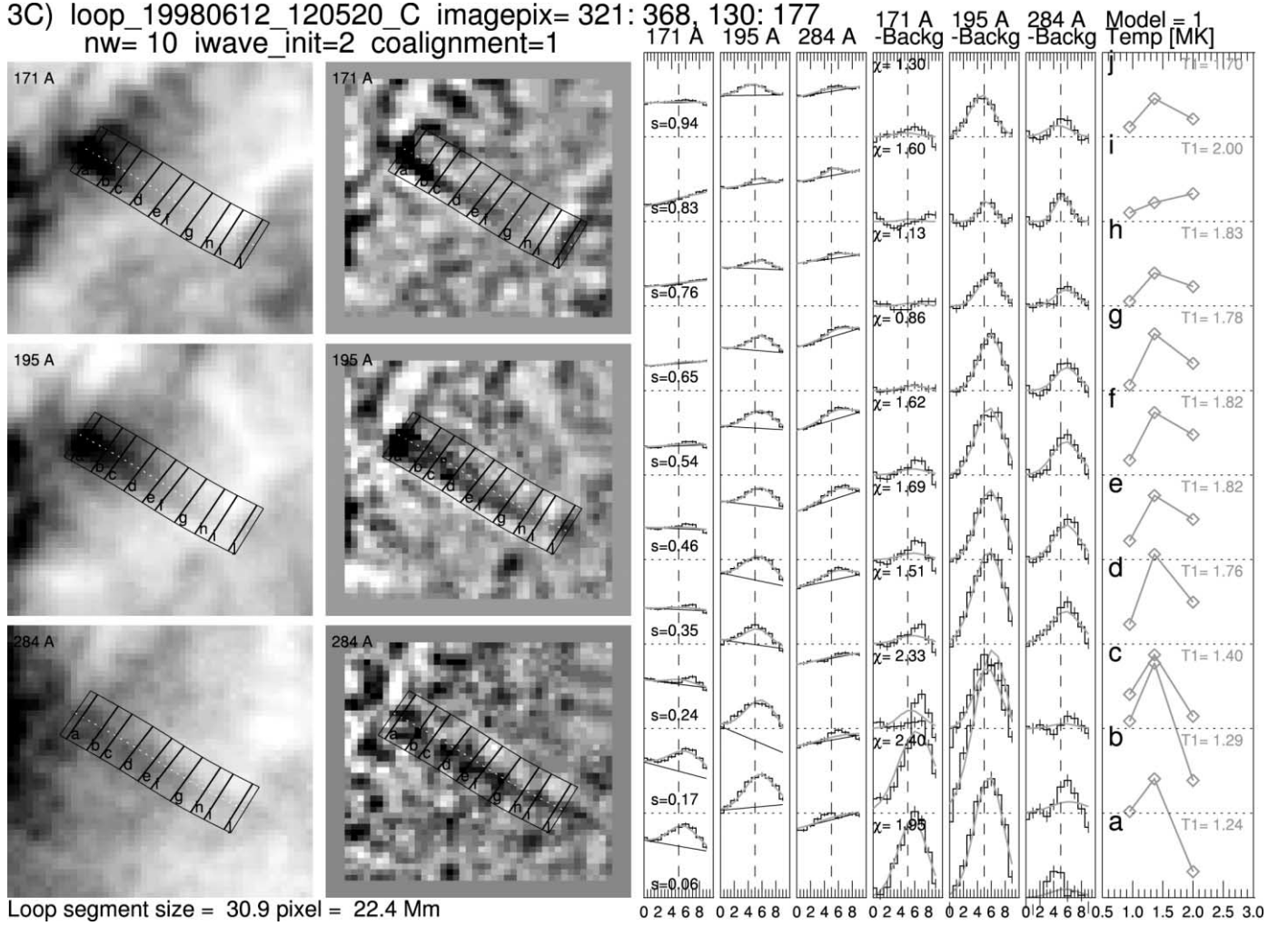


FIG. 6.—Example of data analysis for a hot loop, 3C, observed with *TRACE* on 1996 June 12, 12:05:20 UT. The extracted subimage is in the pixel range [320:379, 121:180]. The representation of the panels is the same as in Fig. 4. See § 3.2 for description.

A selection of 10 cases is shown in Figure 7, demonstrating the temperature diagnostics over the entire sensitivity range of the triple filters, e.g., $0.7 \text{ MK} \lesssim T \lesssim 2.8 \text{ MK}$. The 10 selected cases in Figure 7 are ordered with increasing temperature (*from top to bottom*).

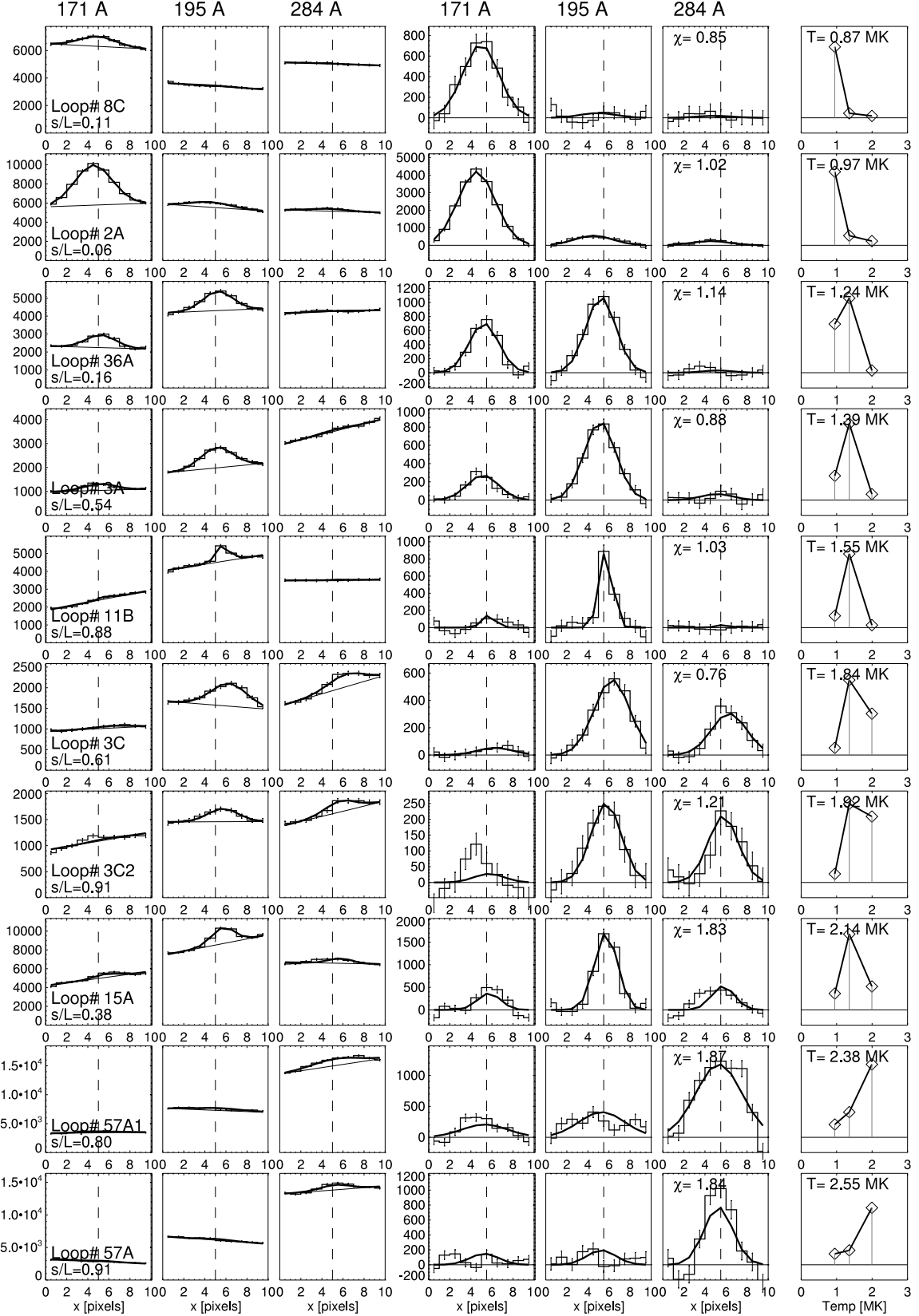
3.3. Isothermal versus Multithermal Model

A central question of our study is the temperature structure of the finest detectable loop strands. The forward fitting with the two models provides us a clear discrimination as to whether the analyzed loop strands are isothermal or multithermal. We show the goodness of the fits (χ_{red}) of both models for all $N = 17,908$ cross-sectional fits in Figure 8, in the form of a scatterplot, with the multithermal model on the x -axis ($\chi_{\text{red},0}$) and the isothermal model on the y -axis ($\chi_{\text{red},1}$). Since the isothermal model represents a special case of the multithermal model, it is contained in it and each acceptable isothermal fit should also lead to an acceptable multithermal fit. This is indeed the case, as evident from the triangular clustering with $\chi_{\text{red},0} \lesssim \chi_{\text{red},1}$ (within some slight scatter). This is an important sanity test that verifies that the convergence behavior of both models is satisfactory.

If all data were noise-free and consistent with an isothermal model, both models should converge to exactly the same solution, and the scatterplot should show a linear relation $\chi_{\text{red},0} \approx \chi_{\text{red},1}$. This is indeed the case for the majority of fits because

many points of the scatterplot in Figure 8 lie near the diagonal line $\chi_{\text{red},0} \approx \chi_{\text{red},1}$. However, because the two models have a slightly different number of free parameters ($n_{\text{free}} = 10$ for the isothermal model vs. $n_{\text{free}} = 11$ for the multithermal model) and because the data are not noise-free and contain also secondary substructures that add to the noise, the two forward fits converge to slightly different best solutions, with slightly different goodness of fit. So, we see that most of the data points lie in a cone of $\chi_{\text{red},0} \approx \chi_{\text{red},1}$ within a factor of ≈ 1.5 (see cone in Fig. 8). Inside this cone we consider both models as equally consistent because the slight difference on the goodness of fit within a factor of 1.5 just results from the noise and contaminating secondary structures, which affect both models equally. Even though we attempted to select isolated and high-contrasting loops uncontaminated by background structures, it cannot be avoided that ambient loops in the foreground or background cross the selected structures at arbitrary positions, for which our geometric model with a single-Gaussian cross section and a linear background is not adequate.

The most interesting part of the scatterplot is the top left corner, where the multithermal model provides a significantly better fit than the isothermal model, say, in the range of $\chi_{\text{red},1} \geq 1.5\chi_{\text{red},0}$. These are the *non-isothermal* cases, while the other multithermal fits (near the diagonal in Fig. 8) contain the subset of *isothermal* cases. If we consider only those cases where a multithermal model



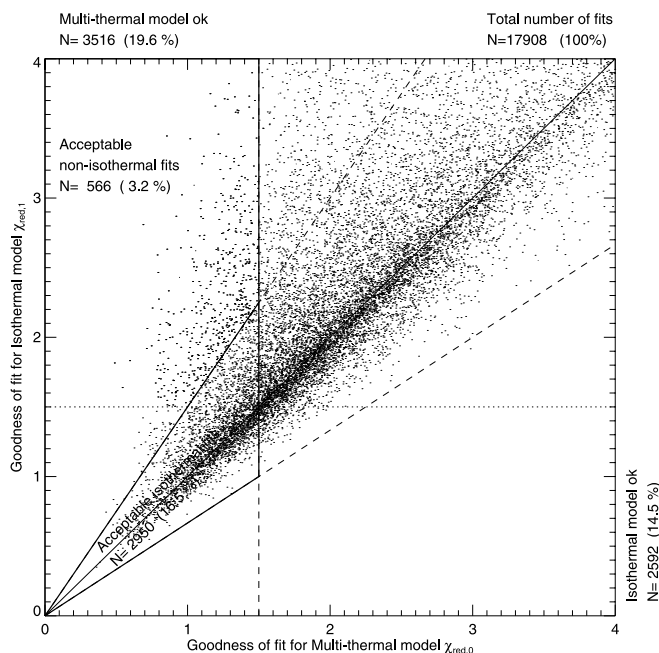


FIG. 8.—Scatterplot of the reduced χ^2 values of the two models that have been forward fitted to $N = 17,908$ loop cross sections. The goodness of the multithermal fit $\chi_{\text{red},0}$ is plotted in the x-axis, and the corresponding value for the isothermal fit $\chi_{\text{red},1}$ on the y-axis. The scatterplot is subdivided into regimes of acceptable fits $\chi_{\text{red},1} \leq 1.5$ for both fits, and the isothermal fits that are inferior to multithermal fits are located in the top left section (3.2% of all cases). The diagonal cone section $\chi_{\text{red},1}/1.5 < \chi_{\text{red},0} < 1.5\chi_{\text{red},1}$ reflects the equivalence between the isothermal model and the special case of the multithermal model where the DEM collapses to a single temperature. In the limit of noise-free data the χ_{red} values of both models would converge to the diagonal line.

yields an acceptable fit, say, in the range of $\chi_{\text{red},0} \leq 1.5$, which is the case for $N = 3516$ fits, we find that $N = 2950$ cases (84%) have an acceptable isothermal fit, while only $N = 566$ cases (16%) have an acceptable non-isothermal fit. Thus, only one in six cases requires a non-isothermal model, while the vast majority is consistent with an isothermal temperature model. Therefore, we conclude that most of the analyzed loop strands are indeed consistent with an isothermal (single temperature) cross section, while the few non-isothermal cases are most likely cases with unresolved nearly coincident loop strands along the same line of sight, often affecting only a short loop segment. This dominance of isothermal fits is an important result with far reaching consequences that is for the first time demonstrated in this study.

In the following we discuss only the results from acceptable isothermal fits, since the non-isothermal model seems not to be relevant in most of the cases.

3.4. Statistics of Fitted Loop Widths

The distribution of loop widths $w = 2.35\sigma_w$ is shown in Figure 9 (*top left panel*). We find that the majority of the FWHM widths of the fitted loops lie in the range of 1000–2000 Mm, with a maximum likelihood at $w_m = 1420 \pm 340$ km, for all fits as well as for the subset of acceptable fits. At the lower side we expect a cutoff at the spatial resolution of 2.5 pixels, which corresponds to 900 km, which indeed constitutes a lower boundary for almost all measured widths. At the upper side we expect a filter cutoff at the width of the boxcar filter we used, which was 7 pixels wide, corresponding to a maximum width of $7 \times 0.5 \times 725$ km = 2540 km. Indeed almost all widths are measured within this range of 900–2540 km (see Fig. 9, *top left panel*).

The detailed shape of the distribution between these two boundaries depends on the intrinsic distribution of loop widths $N(w)$, the selection bias $q^{\text{sel}}(w)$ of the brightest and most contrasting loops we applied, and the smoothing filter $q^{\text{filt}}(w)$. The overall distribution in the range of $w < 2500$ km can be characterized with a normal distribution, with a mean and standard deviation of $w = 1420 \pm 340$ km.

Comparing the distribution of detected loop widths, which have a mean and standard deviation of $w = 1420 \pm 340$ km here, we find that statistics from earlier studies detected all significantly wider loops, e.g., $w = 3670 \pm 1470$ Mm within a total range of 1500–7500 km for 41 *TRACE* loops (Aschwanden et al. 2000b), or $w = 7100 \pm 800$ km for 30 EIT loops (Aschwanden et al. 1999). We detected smaller loop widths here because we used a high-pass filter for their detection, rather than the original unfiltered images (e.g., in Aschwanden et al. 2000b), as well as a higher spatial resolution (*TRACE* vs. EIT).

3.5. Statistics of Loop Lengths

The distribution of loop detection lengths is shown in Figure 9 (*top right panel*), which can be characterized with a mean and standard deviation of $L = 32 \pm 17$ Mm if we neglect the high-end tail at $L > 70$ Mm, which extends up to $L = 120$ Mm. This distribution, however, includes only the loop segments over which a loop could be traced with sufficient contrast, so it represents only a lower limit of the full loop lengths. Most structures represent segments of closed loops, but there are also segments of open field lines included. Given the pixel size of 0.5×725 km = 362 km, the average detected loop segment length extends thus over $32,000/362 = 88$ pixels, which is the reason why we subdivided each loop segment into 80 loop positions, so that the average fitted loop position is about 1 pixel apart, and thus they are independent of each other.

Let us compare these loop detection lengths with earlier measurements. Full loop lengths of $L = 8$ –648 Mm (with a median of $L = 260$ Mm) were evaluated in a study of 41 *TRACE* loops (Aschwanden et al. 2000b). The mean detection length of loop segments is in this study about a factor of 8 smaller because we extracted only the least contaminated segments of loops. In an earlier EIT study loop segments with a mean and standard deviation of $L = 89 \pm 29$ Mm were detected, while the full loop lengths were estimated to be $L \approx 290 \pm 70$ Mm (Aschwanden et al. 1999), so the full loop lengths were comparable with the *TRACE* study, and our detected segments here are about a factor of 3 shorter than in the EIT study. So, we have to be aware that the detection of loop segments here is somewhat shorter than in earlier studies, mostly because we apply the triple-filter fits only to the segments near the footpoints that have a high contrast in the high-pass filtered images, while we ignored the fainter segments near the top of large loops.

3.6. Statistics of Fitted Loop Temperatures

In this study we fitted loop cross sections with a single temperature (for the isothermal model) to the observed flux profiles in the three filters. The distribution of the resulting temperatures T_e is shown in Figure 9 (*second row, left panel*), which shows a peak at $T \approx 1.05$ MK and a secondary peak at $T \approx 2.1$ MK. Although we tried to obtain an unbiased selection of temperatures, we ended up with much more cooler than hotter loops because there was often no high-contrast and unconfused loop structure found in the 284 Å image that was suitable for three-filter fitting. Moreover, the distribution of obtained temperatures turned out not to fall off monotonically with higher temperatures but seems to peak at the temperatures that correspond to the maximum

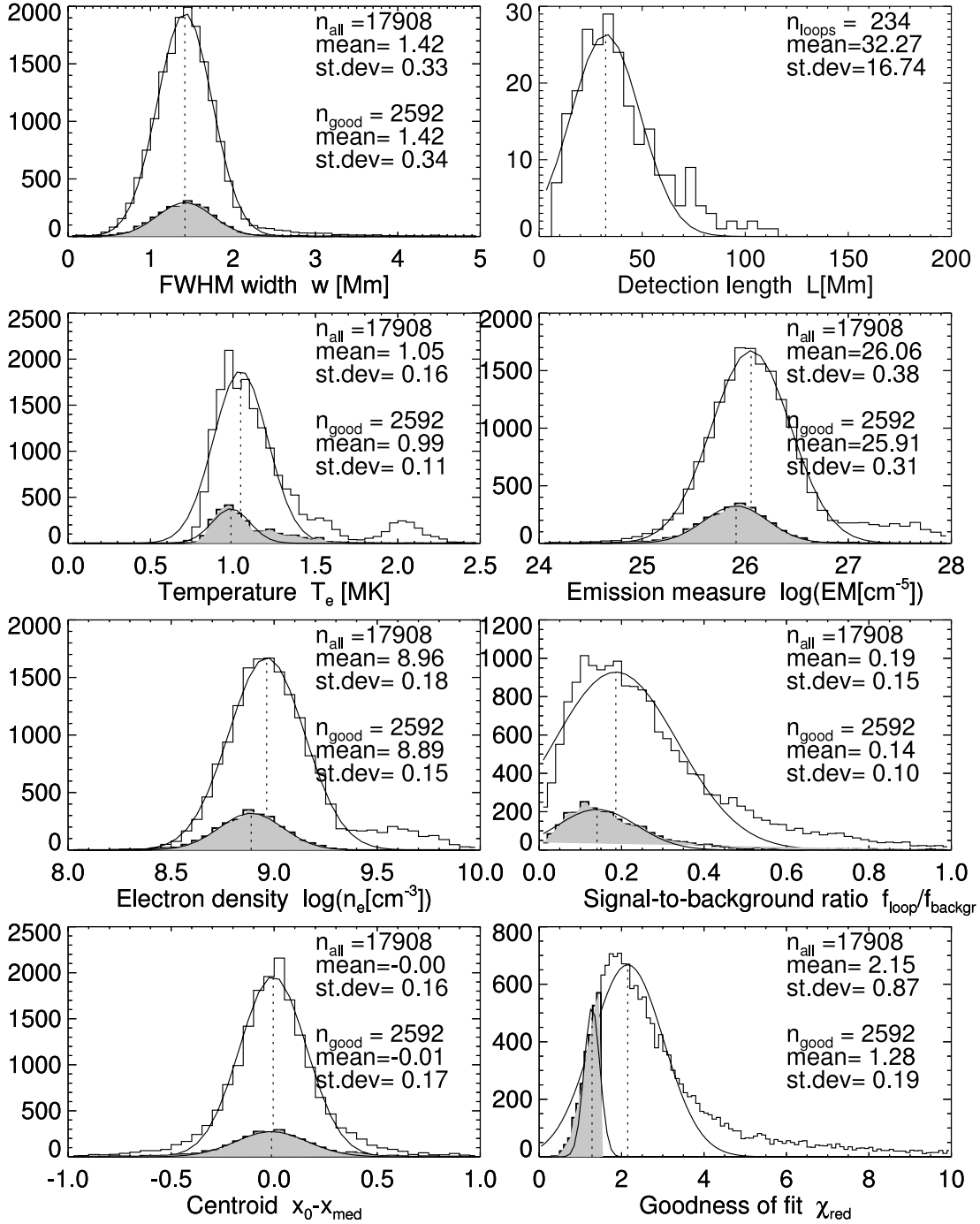


FIG. 9.—Distributions of the best-fit parameters: the FWHM loop width w (top left), the electron temperature T_e (second row, left), the electron density n_e (third row, left), the Gaussian centroid position (bottom left), the loop detection length L (top right), the emission measure EM (second row, right), the signal-to-background ratio or ratio of loop-associated flux to background flux S/B (third row, right), and the goodness of the isothermal fit $\chi_{\text{red},1}$ (bottom right). The white histograms represent the values from all (17,908) cross-sectional fits, while the gray histograms refer to the acceptable fits ($\chi_{\text{red},1} \leq 1.5$) of the isothermal model. The curved functions represent Gaussian fits to the peaks of the distributions, yielding the means and standard deviations indicated in each panel.

sensitivity in the three filters (see response functions in Fig. 2). So, we can represent the obtained distribution of temperatures with a superposition of three Gaussian distributions that peak at $T = 1.05$, 1.4, and 2.1 MK and have Gaussian widths of $\sigma_T \approx 0.12$ MK, with relative amplitudes of 8:2:1 (Fig. 9, second row, left panel). This means that we detected near the peak sensitivity of the 171 Å filter about 8 times more than in the 284 Å filter, and in the 195 Å about 2 times more. Thus, on one side these results indicate that the triple-filter fitting method is able to determine temperatures over the whole range of $T \approx 0.7$ –2.8 MK (as demonstrated in Fig. 7), but that the probability of

detection is highest near the peak response of the filter (i.e., at $|T - T_{\text{peak}}| \lesssim 0.12$ MK), within $\gtrsim 90\%$ of the peak sensitivity, but significantly reduced in the lower sensitivity temperature ranges. This bias is partially due to our selection procedure with preference for the highest contrast loops, which is also dictated by the much higher degree of confusion for fainter loop structures detected in the tails of the response function. It implies also that the temperature spacing of future multifilter imagers should be as close as $(T_{i+1} - T_i) \approx 0.25$ MK in the EUV range (corresponding to a sensitivity of $\gtrsim 90\%$ of the peak response in each filter) to warrant uniform detection probability over a desired temperature range.

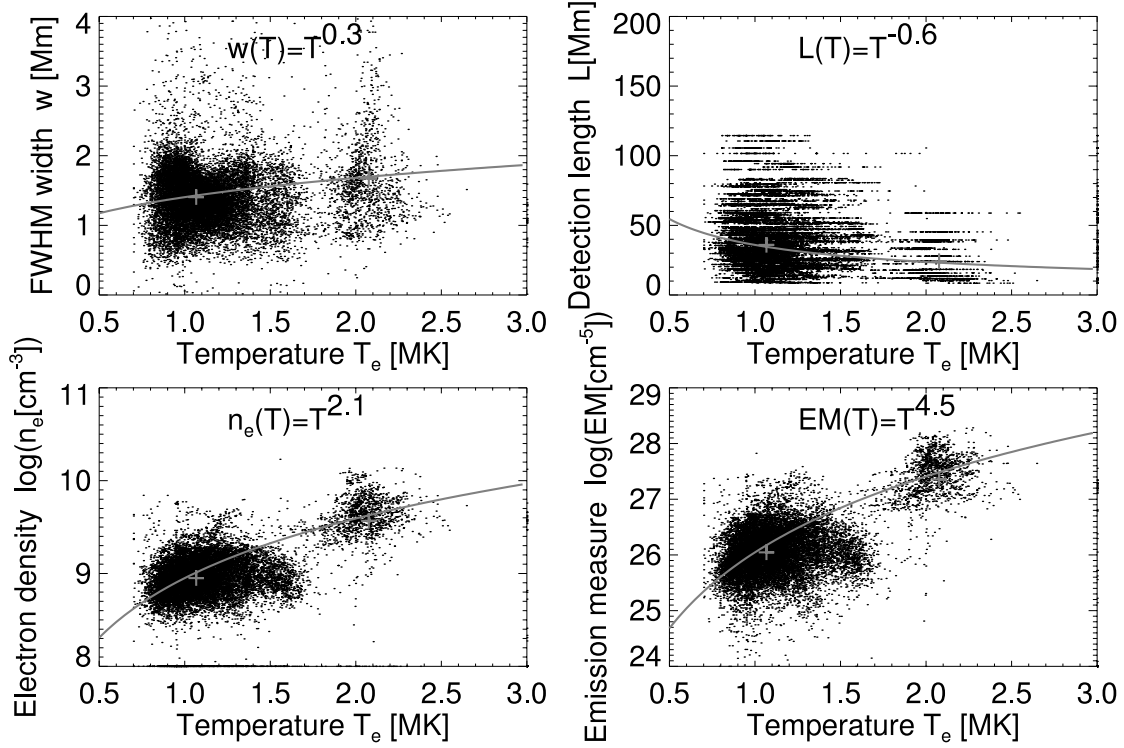


FIG. 10.—Scatterplots of various physical parameters as a function of the temperature: the loop FWHM widths $w(T)$ (top left), the electron density $n_e(T)$ (bottom left), the detection length $L(T)$ (top right), and emission measure $EM(T)$ (bottom right). A linear regression fit of the logarithmic values is indicated in each panel, yielding the power indices of the functional dependencies.

3.7. Statistics of Fitted Loop Emission Measures and Electron Densities

The distribution of emission measures in the detected loop segments is shown in Figure 9 (second row, right panel), which has a mean and standard deviation of $\log EM \approx 25.91 \pm 0.31 \text{ cm}^{-5}$, if we neglect the high-end tail extending from $\log EM \approx 27$ to $\max(\log EM) = 2 \times 10^{28} \text{ cm}^{-5}$. The majority (83%) of loop segments have an emission measure between 10^{25} and 10^{27} cm^{-5} .

Assuming a coronal filling factor of unity and a circular loop cross section, we can infer the electron density of the loop segments from the relation $n_e = (EM/w)^{1/2}$ from the measured emission measure EM and loop FWHM w . From this we find a main distribution of electron densities with a mean and standard deviation of $\log n_e = 8.89 \pm 0.15 \text{ cm}^{-3}$ (Fig. 9, third row, left panel), if we neglect the high-end tail that extends from $n_e \approx 5 \times 10^9 \text{ cm}^{-3}$ to $\max(n_e) = 1.7 \times 10^{10} \text{ cm}^{-3}$. So, the most frequently detected electron density is at $n_e = 10^{8.89} \approx 8 \times 10^8 \text{ cm}^{-3}$.

The inferred electron density shows a clear dependence on the temperature (Fig. 10, bottom left panel), with a typical density range of $n_e \approx 10^{8.5} - 10^{9.5} \text{ cm}^{-3}$ for cooler ($T_e \approx 1.0 - 1.5 \text{ MK}$) loops and a typical range of $n_e \approx 10^{9.5} - 10^{10.0} \text{ cm}^{-3}$ for hotter ($T_e \approx 2.0 \text{ MK}$) loops. A linear regression fit (of the logarithmic values) yields a scaling of (Fig. 10, bottom left panel)

$$n_e(T) \approx T^{2.1} \quad (10)$$

and a corresponding scaling for the emission measure of (Fig. 10, bottom right panel)

$$EM(T) \approx T^{4.5}, \quad (11)$$

which of course is consistent with the relation $EM(T) \approx n_e(T)^2$ by definition. In contrast, the measured loop widths show only a

weak dependence on the temperature (Fig. 10, top left panel), while the loop lengths show a weak dependence (Fig. 10, top right panel),

$$L(T) \approx T^{-0.6}. \quad (12)$$

The scaling of the inferred density with temperature is approximately consistent with the theoretical scaling law for hydrostatic loops, which follows from the Rosner-Tucker-Vaiana (RTV) relation $T_{\max} \approx 1400(pL)^{1/3}$, with the pressure definition $p = 2n_e k_B T$, yielding

$$n_e(T) \approx T^2 \quad (13)$$

if the temperature dependence of the loop lengths is ignored or

$$n_e(T) \approx T^{2.6} \quad (14)$$

if the empirical scaling $L(T) \propto T^{-0.6}$ (eq. [12]) is included.

Comparing the obtained electron densities with earlier statistical loop studies, i.e., $n_e = (1.92 \pm 0.56) \times 10^9 \text{ cm}^{-3}$ for 30 loops detected in 171 \AA with EIT (Aschwanden et al. 1999), $n_e = (2.44 \pm 0.87) \times 10^9 \text{ cm}^{-3}$ for 18 loops detected in 195 \AA with EIT (Aschwanden et al. 2000a), $n_e = (3.12 \pm 1.00) \times 10^9 \text{ cm}^{-3}$ for 17 loops detected in 284 \AA with EIT (Aschwanden et al. 2000a), and $n_e \approx 10^9 \text{ cm}^{-3}$ for 41 loops detected in 171 \AA with TRACE (Aschwanden et al. 2000b), we find that our densities inferred here are fully compatible with the earlier measurements within a factor of 2, i.e., $n_e = (0.8 \pm 0.3) \times 10^9 \text{ cm}^{-3}$ at $T \approx 1.0 \text{ MK}$ and $n_e = (1.9 \pm 0.3) \times 10^9 \text{ cm}^{-3}$ at $T \approx 2.0 \text{ MK}$.

3.8. Signal-to-Background Ratio of Loop Structures

We characterize a signal-to-background ratio by dividing the loop-associated flux f_p by the background flux f_b according to the

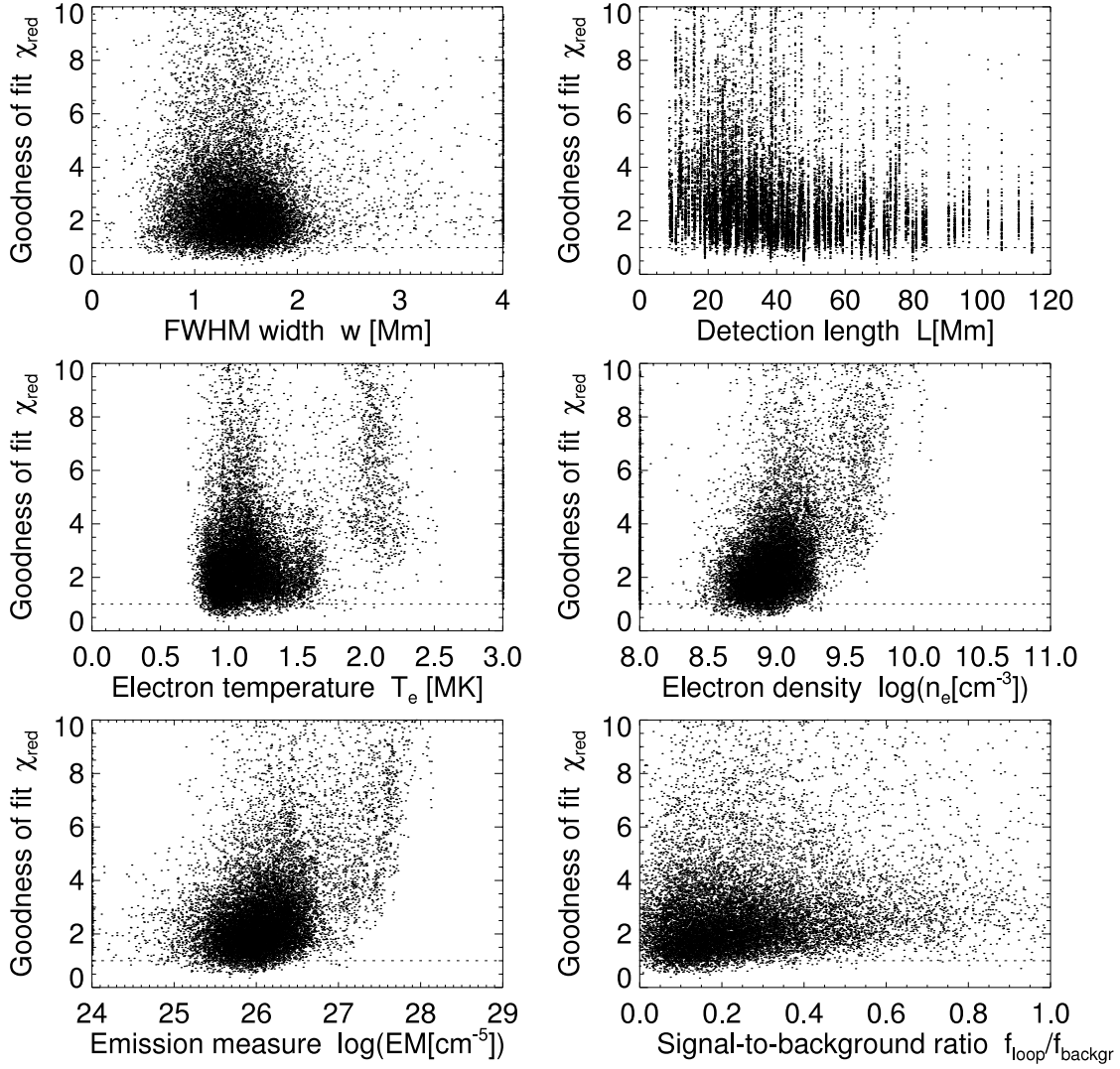


FIG. 11.—Scatterplots of the goodness of fit χ_{red} as a function of six physical parameters. The expectation value of $\chi_{\text{red}} = 1$ (dashed line) represents a lower limit, while the actual values scatter in the range of $1 \lesssim \chi_{\text{red}} \lesssim 4$ for cool ($T \lesssim 1.5$ MK) loops and in the range of $4 \lesssim \chi_{\text{red}} \lesssim 8$ for hotter ($T \gtrsim 1.5$ MK) loops. See discussion in § 3.9.

definition in equations (1) and (2), taken in the filter that is most sensitive to the fitted loop temperature. The distribution of these signal-to-background ratios is shown in Figure 9 (*third row, right panel*), which shows a maximum at $S/B = 14\%$, with a Gaussian distribution of $14\% \pm 10\%$ around the peak. Extremal values are 0.2% at the low end and 165% at the high end. This means that a background variation of $\approx 14\%$ has a comparable influence on the forward fitting as the flux of the loop itself. The background modeling is therefore extremely important in most cases of the selected loops, which has often been inaccurately handled in earlier studies. In this study we pursued the approach of empirical background modeling simultaneously with the loop fitting, using six free parameters for the background fitting in all three filters. Note that this approach of simultaneous loop-plus-background fitting is superior to many other commonly used background treatments, e.g., subtraction of the local flux minima on both sides of a loop and subtraction of a constant background, sometimes evaluated at a different time than the loop fitting. The required accuracy in background modeling is often underestimated because it is often assumed that the background flux is weak compared with the loop flux and that the background flux is well defined. Here, however, we find that the background flux is on average a

factor of 6 larger than the loop flux in the most sensitive filter, if one selects the finest resolved loop strands.

3.9. Goodness of χ^2 Fit

The success or failure of the forward fitting of a parameterized model to observed data can only be evaluated from a quantitative measure of the difference between model and data, which we quantify by the goodness of χ^2 fit, in terms of the reduced χ^2 as defined in equation (9). We show scatterplots of the χ_{red} values (per loop) as a function of various physical parameters in Figure 11, in order to understand trends that affect the fit quality of the model. We see that the goodness of the fits is generally in the range of $1 \lesssim \chi_{\text{red}} \lesssim 4$ (Fig. 9, *bottom right panel*; Fig. 11). A fraction of 14.5% has acceptable fits with $\chi_{\text{red}} \leq 1.5$ for the isothermal model, while a fraction of 78.8% cannot be fitted with an acceptable χ_{red} with either temperature model (Fig. 8).

There are a number of factors that affect the calculation of the χ^2 that are not fully accounted for here. For the estimate of the standard deviation of photon counts in a given pixel and exposure time interval we included only the Poisson statistics of the photon counts (eq. [8]). We neglected other noise contributions,

such as the CCD readout noise, the digitization noise, the lossless JPEG compression noise, the pedestal/dark current, the integer subtraction, and (cosmic ray or magnetospheric particle) spike residuals, because they are all small compared with the Poisson noise of the photon counts, except for the spike residuals (see detailed quantification of various noise factors in Aschwanden et al. 2000c). We did not include the noise from spikes because it is very variable from case to case, depending on the orbit position, exposure time, and removal technique. Many loops are not affected by such spikes because the extracted spike represents only a very small fraction of a total image. We did also refrain from spike filtering because it could also remove parts of the finest loop strand structures that are the main object of our study. Moreover, if a spike coincides with a loop cross section where a fit is performed, the forward fit will be so bad that it automatically would be discriminated by an excessive χ_{red} or an inconsistent centroid position $x_0 - x_{\text{med}}$ or loop width w . So, spikes do not need to be included in the estimate of the standard deviation of the fit because they reveal themselves with an excessive χ_{red} value.

The most likely reason for the higher χ^2 values (in the range of 1–4) instead of the theoretically expected ideal range (of ≈ 1) is contamination from foreground and background loops, in particular in filters that are not sensitive to the primary selected loop. For a loop that has, say, a temperature of $T \leq 1.0$ MK, most of the loop-associated flux is detected in the 171 Å filter, only $\leq 16\%$ in the 195 Å channel, and basically nothing ($\leq 2\%$) in the 284 Å filter (see response functions in Fig. 2). It is likely that there are other secondary (non-cospatial) loops visible in the 195 and 284 Å images, which bring the χ^2 values up to 2–4 standard deviations from the (linear) background model. So, the χ^2 of the best fit could possibly be improved by including more free parameters in the background model, in particular in the filters that are not sensitive to the primary selected loop, or alternatively by excluding those filters in the χ^2 calculation. Because most structures are generally visible in the 171 Å images, the confusion by secondary loops is therefore most severe for loops of $T \gtrsim 2$ MK because they cause large standard deviations from a linear background model in the 171 Å image, while the primarily fitted loop dominates in the 195 and 284 Å images only. This is the reason why the χ^2 values for all loops with hot temperatures are generally higher, say, in the range of $3 \lesssim \chi_{\text{red}} \lesssim 8$ (for statistics see Fig. 11, *middle left panel*; or for a single case see Fig. 6). Of course, the fit could also be improved by simultaneous fitting of multiple loop strands. The correlations of the goodness of fit χ_{red} with the electron density (Fig. 11, *middle right panel*) and emission measure (Fig. 11, *bottom left panel*) are a consequence of the scaling law between temperature, density, and emission measure (eqs. [10], [11], and [13]).

A third reason for the high χ^2 values could be the inadequacy of the theoretical model (i.e., a Gaussian shape of the loop cross section). We would expect that the model is not sensitive to the detailed shape of the observed loop cross section profile for low counts, but more sensitive for high counts with better Poisson statistics. Therefore, we expect an increase of the χ^2 value for the goodness of the fit with increasing flux or emission measure, which is similar to the scaling law between temperature, density, and emission measure (eqs. [10], [11], and [13]) and thus cannot easily be discriminated from the previously discussed effect of increased low-temperature background contamination for hotter loops. The correlations of the goodness of fit with temperature, electron density, and emission measure as evident from Figure 11 can therefore be interpreted by both effects.

We will expand our forward fitting technique by increasing the number of free parameters in theoretical models in future papers, in order to adjust for non-Gaussian loop cross sections, deviations from linear backgrounds, and multiple loop strands with different temperatures. This should help to reduce the goodness of fit for both effects discussed above.

4. DISCUSSION

4.1. Problems with Resolving Loop Strands in Earlier Studies

According to our analysis, we found that the loop-associated EUV flux of elementary single-temperature loop structures has a typical FWHM of 1–2 Mm and a signal-to-background ratio of only $\approx 5\%$ – 25% . This means that the loop-related flux counterparts in images with different temperature filters can only be properly extracted if (1) a multifilter instrument has a spatial resolution of $\lesssim 1''$, so that the cospatiality of loop structures can be determined with an accuracy of a fraction of an arcsecond, and if (2) the loop-unrelated background flux is subtracted with an accuracy of a few percent. These strict requirements have not been met in most previous studies on coronal loops, and thus the attempted determinations of temperatures represent statistical averages of ensembles of loop strands or mixtures of selected loops and background structures. The often-quoted claim of “loop extraction after careful background subtraction” is not credible unless the authors show explicitly a cross-sectional loop flux profile including the background profile in all analyzed temperature filters, so that the reader can test the cospatiality and confusion by adjacent or background loop structures. Once a loop structure is credibly isolated and resolved in multiple filters, a temperature determination based on filter ratios of the loop-associated flux should lead to a reliable temperature value (if the filter ratio is unique), while a forward fitting technique would be more preferable (if the loop profile can be parameterized adequately).

Let us review some earlier studies and point out some problems with their temperature diagnostics, based on the insights we obtained after this new study here. Multifilter studies of a coronal loop have been performed with up to 19 different temperature filters in the temperature range of $T = 0.25$ – 2.5 MK with CDS (e.g., Schmelz et al. 2001), but since the used pixel size is $4''$ (2900 km), the obtained differential emission measure (DEM) distribution $\text{DEM}(T)/dT$ reflects a statistical distribution over an ensemble of elementary loop strands (which have typical widths of 1000–2000 km according to our study here). Unfortunately, any information on the cospatiality of the analyzed loops in different temperature filters is lacking in most of these studies (Schmelz et al. 2001, 2003), so that we do not know their spatial displacement in different filters. However, it is not surprising that the broad DEM distribution found from CDS is not consistent with a single temperature (Schmelz 2002; Martens et al. 2002) because this finding of a broad DEM was erroneously attributed to a *single loop* rather than to an *ensemble of loops or strands* (as it would have been obvious after measuring the spatial displacements in different temperatures).

A triple-filter study has been undertaken with EIT 171, 195, and 284 Å filters for 10 loops (Schmelz et al. 2003). However, since the pixel size of EIT is $2''.6$ (1900 km), the analyzed structures consist of multiple elementary loop strands (which are found to have typical widths of 1000–2000 km here). Another clear indicator that each so-called loop structure includes an overwhelming contribution of background in that EIT study is the signal-to-background ratio of the analyzed loops. A total of 10 loop structures were analyzed at five positions each, and the

total fluxes f and background fluxes b are listed in Table 2 of Schmelz et al. (2003). We calculate the signal-to-background ratio $S/B = (f - b)/b$ from their Table 2 for the 171 Å filter and find a median value of $S/B = 104\%$, or a mean and standard deviation of $S/B = 168\% \pm 153\%$, which is more than an order of magnitude higher than for elementary loop strands analyzed here ($S/B = 14\% \pm 10\%$). Thus, all temperature determinations in this EIT study (Schmelz et al. 2003) are not attributable to single (resolved) loop strands but refer to statistical ensembles of loops from the background corona.

A detailed study of a single loop with both *TRACE* and *SOHO* CDS instruments has been presented by Del Zanna & Mason (2003). The analyzed loop was found to have a width of 8'' (5800 km) and a signal-to-background ratio of $(f - b)/b = 76\% \pm 34\%$ in the 171 Å filter. The authors find that the loop cross sections are isothermal with temperatures of $T \approx 0.7\text{--}1.1$ MK. However, the measured width and signal-to-background ratio are significantly larger than for the loop strands measured here, so that we conclude that it represents an ensemble of loop strands with similar temperatures. The filamentary structure of a few coronal loops has also been addressed in a two-filter *TRACE* study, but since widths in the range of $w = 4000\text{--}20,000$ km have been found, what are called “fibrils” therein (Testa et al. 2002), we conclude that each of those fibrils contains an ensemble of many loop strands analyzed here (with widths of $w \approx 1000\text{--}2000$ km).

Also, the EIT study on 30 loop structures of Aschwanden et al. (1999) shows much larger widths ($w = 7100 \pm 800$ km) and signal-to-background ratios [$(f - b)/b \approx 10\%\text{--}50\%$] than for the loop strands analyzed from *TRACE* here and thus are likely to consist of multiple loop strands. A subsequent *TRACE* study on 41 coronal loops (Aschwanden et al. 2000b) shows loop widths of $w = 3670 \pm 1470$ km, which are about a factor of 2 larger than the loop strands analyzed here and thus are also likely to include contaminations from adjacent loops. An important aspect in the method of resolving elementary loop strands is the use of a high-pass filter, which allowed us to localize loop strands with widths of $w \lesssim 2000$ km here, while we localized only groups of loop strands with widths of $w \lesssim 5000$ km in the previous *TRACE* study without using a high-pass filter (Aschwanden et al. 2000b).

In summary, all previous studies showed significantly larger loop widths and a much higher signal-to-background ratio (defined as the ratio of loop-associated flux to background flux) and thus represent an ensemble of loop strands, which is equivalent to a multitemperature structure. Our present study provides a new criterion for elementary loop strands that have a single temperature across their cross section: (1) they have typical widths of $w \lesssim 2000$ km and (2) they have signal-to-background ratios of $S/B = (f - b)/b \approx 5\%\text{--}25\%$.

We illustrate the measurements with different instruments in Figure 12. Assuming that a coronal structure consists of multiple elementary strands, we simulated the superposition of 20 strands with random widths ($w = 920 \pm 650$ km), random positions ($x_0 = 15 \pm 5$ Mm), and random fluxes (Fig. 12, *top panel*). Then we resampled the simulated cross-sectional flux profile with the pixel sizes of different instruments: *SOHO* CDS with 4'', *SOHO* EIT with 2''.6, and *TRACE* with 0''.5. The resulting FWHM of the peak structure and signal-to-background ratio are then found to be $w = 5800$ km and $S/B = 100\%$ for *SOHO* CDS (Fig. 12, *second panel*), $w = 5600$ km and $S/B = 100\%$ for *SOHO* EIT (Fig. 12, *third panel*), and $w = 1800$ km and $S/B = 20\%$ for *TRACE* (Fig. 12, *bottom panel*), similar to the values reported in the literature.

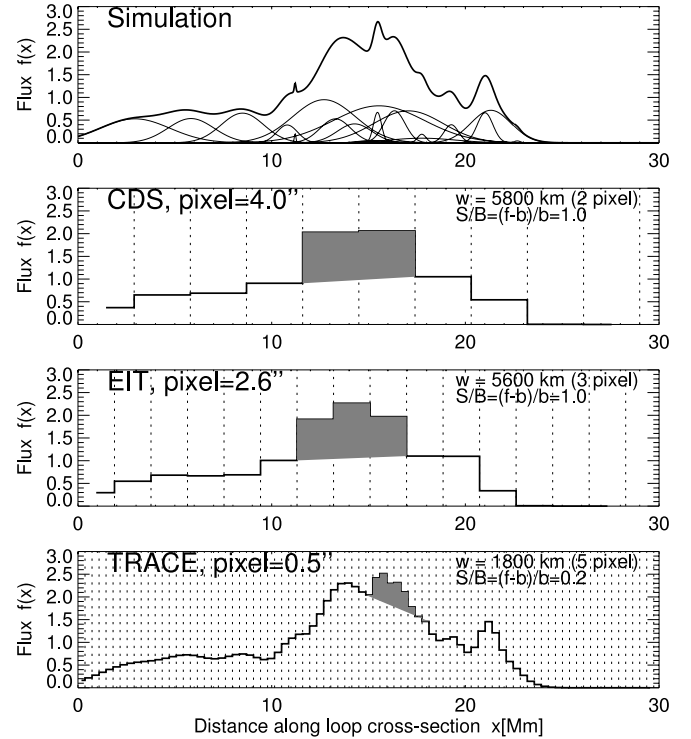


FIG. 12.—Simulation of 20 superimposed loop profiles (*top panel*), rebinned to the pixel size of CDS (*second panel*), EIT (*third panel*), and *TRACE* (*bottom panel*). The peak is background subtracted in each profile (*gray area*), which shows the progressively smaller detected width w and smaller signal-to-background ratio S/B with increasing instrumental resolution.

4.2. The Isothermality of Loop Cross Sections

The next important question is whether the loop strands we detected in this study, with FWHM of $w \approx 1000\text{--}2000$ km, represent elementary strands with a single temperature over their cross section or, alternatively, ensembles of finer strands. We are aware of the lower cutoff at $w \approx 900$ km due to the spatial resolution (or instrumental point-spread function), which prevents us from seeing smaller strands. Nevertheless, we can ask the question whether strands with $w \lesssim 2000$ km are isothermal in their cross section or not.

Our results show that a single-temperature fit is fully consistent with the data, as long as the primary selected loop can be isolated and is little confused by secondary structures. We achieved 2592 forward fits with a $\chi_{\text{red}} \leq 1.5$, while all others out of the 17,908 loop cross section fits show a higher χ_{red} because of the discussed contamination of loops visible in filters that are not sensitive to the temperature of the primary selected loop, and most of those could not be fitted with any multithermal model (with the same geometric parameterization) either. In other words, the cases for which the multithermal model (which includes also the isothermal model) does not lead to an acceptable fit ($\chi_{\text{red}} \leq 1.5$) cannot be fitted with any alternative parameterization of the thermal structure but require a more complex geometric model. This can also be seen most clearly in the examples shown in Figures 4 and 6. The best fit in Figure 4 occurs at loop position h (at $s/L = 0.75$) with $\chi_{\text{red}} = 1.19$, but it worsens to $\chi_{\text{red}} = 1.93$ at the neighbored position g (at $s/L = 0.85$), where secondary structures become visible in the 284 Å filter. Likewise, the best fit in Figure 6 occurs at loop position g (at $s/L = 0.65$) with $\chi_{\text{red}} = 0.86$, while it worsens to $\chi_{\text{red}} = 1.5\text{--}2.4$ at positions $a\text{--}d$ (at $s/L = 0.04\text{--}0.35$) where a secondary loop appears in the 171 Å filter, with a peak that is 2 pixels displaced to the primary loop.

So, we can say that all the detected loop structures we identified with widths of $w \lesssim 2000$ km are consistent with a single temperature in their cross section, but in many cases an acceptable fit could not be obtained because of contaminating secondary structures that cannot be accommodated with our minimum-parameter geometric model (which contains only a single-Gaussian profile and linear backgrounds).

4.3. Do We Resolve Elementary Loop Strands?

Because of the instrumental point-spread function limit, we cannot resolve loops with smaller widths than $w \approx 900$ km, so we cannot exclude that there exist many finer strands. However, if we adopt the definition of an elementary loop strand in terms of a homogeneous temperature cross section, all of the detected structures here, with widths of $w \approx 1000$ – 2000 km, qualify as elementary structures because we found them to be consistent with a single-temperature model. Theoretically, they could be further subdivided with finer strands of equal temperature with some filling factor (model UMI in Fig. 1), but it is very unlikely that multiple adjacent strands that are thermally insulated would be all heated to exactly the same temperature and maintain their temperature in synchrony. Therefore, it is the weakest assumption to assume that an isothermal cross section consists of a single plasma column that has been filled uniformly with plasma from the same source with equal pressure and temperature. If the pressure would change over the loop cross section with equal temperature, the density would change correspondingly and the radiative cooling times ($\tau_{\text{rad}} \propto T_e/n_H$) would change over the cross section, leading to a temperature differential that violates the assumption of an isothermal cross section in the first place. In summary, we conclude that the observed loop strands with widths of $w \approx 1000$ – 2000 km are consistent with an isothermal cross section and thus represent *elementary strands* in terms of thermal homogeneity.

4.4. Consequences for the Heating of Coronal Loops

Our result that coronal loop strands with diameters of $w \lesssim 2000$ km have an isothermal cross section (also called *monolithic* flux tubes) implies a uniform spreading process of heated coronal plasma over this cross section. However, since cross field transport is strongly inhibited in the solar corona due to the low plasma β parameter less than unity (e.g., $\beta = p_{\text{th}}/p_{\text{mag}} < 1$), especially in active regions where most of the heated loops are seen, either (1) the heating process has to occur uniformly over this cross section in the corona, or (2) the heating occurs in a region with cross field transport, such as in the chromosphere. Since the first possibility requires a high degree of organization in the spatial heating function, we think that the second possibility is much more likely. If the coronal loops are heated in the upper chromosphere, where the higher plasma β , higher resistivity, and turbulence occur, cross field transport is possible that spreads the heated plasma over a larger area, aided also by the canopy-like magnetic field expansion that occurs in the transition region. The heated plasma that flows in the upward direction due to the strong negative pressure gradient will then be distributed over a larger loop cross section above the magnetic canopies.

Since the photosphere is structured by subphotospheric convection cells with typical diameters of $d \approx 1000$ km, the photospheric plasma is convected to the intergranular lanes, which have a typical distance of two granulation cells ($2d \approx 2000$ km), which also organizes the vertical magnetic field into bundles that are anchored in the intergranular lanes and spread out to flux tubes with an average diameter of $w \lesssim 2000$ km in the transition region

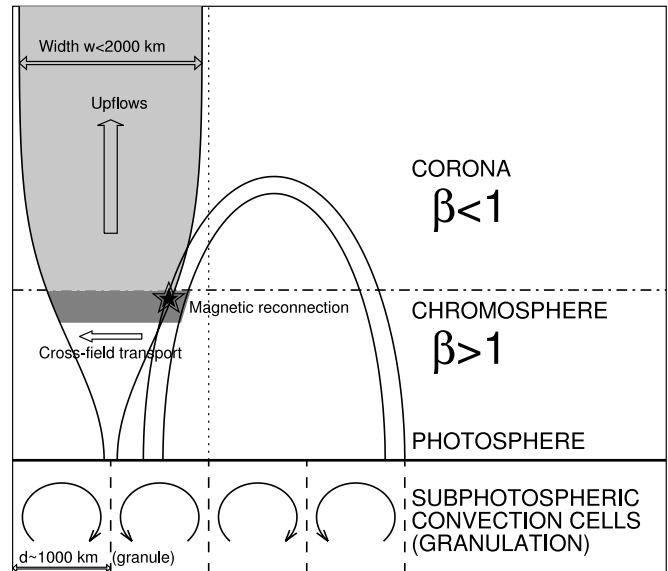


FIG. 13.—Sketch of a theoretical model that explains the thermal homogeneity of coronal loops for widths of $w \lesssim 2000$ km, based on the magnetic field expansion from intergranular photospheric locations. The heated plasma is uniformly spread over the entire loop cross section at a height where the plasma β parameter exceeds the value of unity, say, in the upper chromosphere or lower transition region.

(Fig. 13). This expansion of magnetic flux tubes with height in the upper chromosphere and transition region is similar to the canopy effect that has been proposed for supergranules (Gabriel 1976) but occurs also on a smaller scale for granules. This geometry explains naturally that coronal flux tubes with widths of $w \lesssim 2000$ are uniformly filled with heated plasma, requiring only heating below the altitude (where $\beta \gtrsim 1$) and overpressure-driven upflows, similar to the *chromospheric evaporation* process in solar flares. The heating process could be accomplished by magnetic reconnection either (1) in the transition region or (2) in coronal heights, provided that the heating is coupled downward to the transition region (by either thermal conduction fronts or non-thermal particles like in solar flares). The former possibility could be accomplished by twisting and braiding introduced by random footpoint motion, driven by subphotospheric convection flows (e.g., Parker 1983).

5. CONCLUSIONS

In this study we analyzed 234 coronal loops detected in *TRACE* triple-filter data at wavelengths of 171, 195, and 284 Å. We selected a representative set of the thinnest loop structures, with high contrast and possible isolation from contaminating foreground and background loops, detected with a (boxcar) high-pass filter that enhances loop structures with a width of $w \lesssim 7$ pixels = $3''.5 = 2540$ km. We extracted 17,908 cross-sectional flux profiles from the 234 loops and forward fitted a multithermal and an isothermal model to the flux profiles extracted in the three filters, both models characterizing the loop cross-sectional flux profile with a Gaussian function and the background with a linear function in each filter.

The forward fitting models provide either a differential emission measure distribution $\text{DEM}(s)/dT$ (for the multithermal model) or a single emission measure $\text{EM}(s)$ with a single temperature $T(s)$ (for the isothermal model) along the loop coordinate s , along with the loop widths $w(s)$ and corresponding electron densities $n_e(s)$. This is the first systematic study of coronal loop

strands, carried out with *TRACE* triple-filter data and comprehensive statistics, subject to a spatial resolution of $1''25 = 900$ km and a temperature coverage over the range of $T = 0.7\text{--}2.8$ MK. From the data analysis results we make the following main conclusions:

1. The statistical distribution of loop widths has a mean and standard deviation of $w \approx 1400 \pm 300$ km, bound by the instrumental resolution of 900 km at the lower end and by the maximum high-pass filter cutoff of 2540 km at the upper end. Most of the loops are found in the range of $w \approx 1000\text{--}2000$ km, which is significantly smaller than any previous analysis, e.g., $w \approx 3700 \pm 1500$ km from *TRACE*, or $w = 7100 \pm 800$ km from EIT. The identification of smaller loops here is a consequence of the higher spatial instrumental resolution and the use of a high-pass filter. We cannot exclude whether there exist loop strands with finer widths of $w < 900$ km.

2. The signal-to-background ratio, defined here as the ratio of loop-associated flux to the background flux, i.e., $S/B = (f - b)/b = 14\% \pm 10\%$, is found to be much smaller than found in previous studies, e.g., $S/B = 168\% \pm 153\%$ in an EIT study, $S/B = 76\% \pm 34\%$ in a *TRACE* CDS study, or $S/B = 30\% \pm 20\%$ in a *TRACE* study. The much smaller signal-to-background ratios and smaller loop widths detected in this study indicate that we isolated much fainter loop strands, while virtually all earlier studies detected ensembles of (near cospatial) loop strands (see simulation in Fig. 12).

3. Our forward fitting method ensures that we strictly fit cospatial loop strands in all three filters. The fitted centroid positions of the Gaussian loop profiles were found to be cospatial within less than half a pixel (170 km). We find that the observed fluxes can be fitted with a single-temperature model in almost all cases (84%) of the acceptable multithermal fits, while a non-isothermal model provided a better fit only in 16% of the cases. The cases with unacceptable multithermal fits require more complex geometric models to accommodate the contamination from secondary loops in the foreground and background along the same lines of sight, in particular in filters that are not sensitive to the temperature of the primary selected loop.

4. The range of obtained temperatures covers the full range of $T = 0.7\text{--}2.8$ MK. We detected 8 times more (suitable) loops at temperatures of $T = 1.0$ MK than at 2.0 MK, and the probability for detection is highest near the peak sensitivity of each filter ($T = 1.05 \pm 0.12$, 1.4 ± 0.12 , and 2.0 ± 0.12 MK). So, *TRACE* triple-filter data are adequate to determine temperatures over the range of $T = 0.7\text{--}2.8$ MK, but the detection probability is not uniform in temperature. For future instruments, a temperature filter spacing of $T_{i+1} - T_i = 0.25$ MK is recommended, instead of the currently available spacing of $T_{i+1} - T_i \approx 0.5$ MK.

5. The result that all uncontaminated loops with widths of $w \lesssim 2000$ km are consistent with a single-temperature cross section leads us to the conclusion that we indeed resolve *elementary* or *monolithic* loop strands with *TRACE*, in terms of thermal homogeneity over the cross section. Since cross field transport is inhibited in the corona (due to the low plasma β parameter, $\beta < 1$), our result implies that the heating occurs in the transition region or chromosphere where cross field transport is possible (due to higher resistivity, turbulence, higher plasma β values, and magnetic field expansion). The overpressure from these regions then drives upflows that fill the connected coronal flux tubes. Since the expansion of vertical magnetic flux tubes extends over about two granule convection cells (each with a size of $d \approx 1000$ km), we can explain the temperature homogeneity of coronal loops up to widths of $w \lesssim 2000$ km.

This study represents the first quantitative study of loop strands and has clearly demonstrated that we resolve isothermal (monolithic) loop strands in the solar corona with EUV imagers that have a resolution of $\lesssim 1''$, such as with *TRACE*, while all other loop studies with instruments that have a spatial resolution of $\gtrsim 2''$, such as *SOHO* EIT, *Yohkoh*, and *SOHO* CDS, consequently describe an ensemble of loop strands. The term “coronal loop” in the traditional nomenclature is not well defined in its cross-sectional properties. Tacitly it is assumed that a coronal loop has a homogeneous cross section, while inhomogeneous structures are generally specified in terms of a filling factor. Here we can place a spatial scale on the cross-sectional size of homogeneous cross sections. Also the traditional notion of “background flux” is not well defined. Here we arrive at a new meaning in the sense that the coronal EUV flux represents an unresolved *sea* of a multitude of loop strands from the background corona. The isolation of a loop strand therefore strongly depends on the background modeling, and the claim of isolating a single strand from the background is only credible if the cospatiality, spatial scale, signal-to-background ratio, and isothermality are properly quantified in each filter image.

We thank the following colleagues for valuable discussions: Karel Schrijver, Jim Klimchuk, Helen Mason, Joan Schmelz, Fabio Reale, Giovanni Peres, Julio Del Zanna, Amy Winebarger, and Harry Warren, in particular during the *Coronal Loop Modeling* workshops in Paris, France (2002 November 13–15) and in Palermo, Sicily (2004 August 1–3). Also we acknowledge the constructive comments from the anonymous referee. Part of this work was supported by NASA contract NAS5-38099 (*TRACE* mission).

REFERENCES

- Arnaud, M., & Raymond, J. 1992, *ApJ*, 398, 394
 Aschwanden, M. J. 2004, *Physics of the Solar Corona—an Introduction* (New York: Springer)
 Aschwanden, M. J., Alexander, D., Hurlburt, N., Newmark, J. S., Neupert, W. M., Klimchuk, J. A., & Gary, G. A. 2000a, *ApJ*, 531, 1129
 Aschwanden, M. J., Newmark, J. S., Delaboudiniere, J. P., Neupert, W. M., Klimchuk, J. A., Gary, G. A., Portier-Fornazzi, F., & Zucker, A. 1999, *ApJ*, 515, 842
 Aschwanden, M. J., Nightingale, R. M., & Alexander, D. 2000b, *ApJ*, 541, 1059
 Aschwanden, M. J., Tarbell, T., Nightingale, R., Schrijver, C. J., Title, A., Kankelborg, C. C., Martens, P. C. H., & Warren, H. P. 2000c, *ApJ*, 535, 1047
 Chae, J., Park, Y. D., Moon, Y. J., Wang, H., & Yun, H. S. 2002, *ApJ*, 567, L159
 Del Zanna, G., & Mason, H. E. 2003, *A&A*, 406, 1089
 Feldman, U. 1992, *Phys. Scr.*, 46, 202
 Gabriel, A. H. 1976, *Philos. Trans. R. Soc. London*, A281, 399
 Golub, L., et al. 1999, *Phys. Plasmas*, 6, 2205
 Handy, B. N., et al. 1999, *Sol. Phys.*, 187, 229
 Martens, P. C. H., Cirtain, J. W., & Schmelz, J. T. 2002, *ApJ*, 577, L115
 Parker, E. N. 1983, *ApJ*, 264, 642
 Reale, F., & Peres, G. 2000, *ApJ*, 528, L45
 Schmelz, J. T. 2002, *ApJ*, 578, L161
 Schmelz, J. T., Beene, J. E., Nasraoui, K., Blevins, H. T., Martens, P. C. H., & Cirtain, J. W. 2003, *ApJ*, 599, 604
 Schmelz, J. T., Scopes, R. T., Cirtain, J. W., Winter, H. D., & Allen, J. D. 2001, *ApJ*, 556, 896
 Testa, P., Peres, G., Reale, F., & Orlando, S. 2002, *ApJ*, 580, 1159
 Warren, H. P., Winebarger, A. R., & Hamilton, P. S. 2002, *ApJ*, 579, L41
 Warren, H. P., Winebarger, A. R., & Mariska, J. T. 2003, *ApJ*, 593, 1174
 Winebarger, A. R., & Warren, H. P. 2004, *ApJ*, 610, L129
 Winebarger, A. R., Warren, H. P., & Mariska, J. T. 2003a, *ApJ*, 587, 439
 Winebarger, A. R., Warren, H. P., & Seaton, D. B. 2003b, *ApJ*, 593, 1164